ISSN 0915-633X

NATIONAL INSTITUTE FOR FUSION SCIENCE

Effects of Nonclassical Ion Losses on Radial Electric Field in CHS Torsatron/Heliotron

H. Sanuki, K. Itoh and S.-I. Itoh

(Received – Jun. 16, 1992)

NIFS-160 July 1992

RESEARCH REPORT
NIFS Series

NAGOYA, JAPAN

Effects of Nonclassical Ion Losses on Radial Electric Field in CHS Torsatron/Heliotron

Heiji Sanuki, Kimitaka Itoh and Sanae-I. Itoh,

National Institute for Fusion Science,

Furocho, Chikusaku,

Nagoya, 464-01, Japan

ABSTRACT

A selfconsistent analysis is discussed to determine the radial electric field and loss cone boundary in torsatron/heliotron plasmas under the influence of nonclassical ion losses. Effects of the loss cone loss, charge exchange loss of fast ions with neutrals, and the bipolar part of anomalous loss are taken into account. Analysis is applied to the NBI heated plasma in the CHS device. Comparison is made between theoretical results and experimental observations. The increased ion particle losses by the orbit loss and charge exchange loss with neutrals make the radial electric field more negative than the value of purely neoclassical calculation. The partition of the injection energy among the shine through, direct orbit loss, charge exchange loss and bulk heating is estimated by using the self-consistent electric field profile. The power loss of fast ions caused by the orbit loss or charge exchange process is by a facter of several tens to hundred greater than the reduction of the energy loss of bulk ions through the enhancement of radial electric field. Comparison with W7-A experiment is made, and the differences are discussed.

Keywords : radial electric field, CHS torsatron/heliotron, neoclassical, fast ion orbit loss, charge exchange loss, anomalous loss, energy partition.

§ 1. Introduction

Recently, the radial electric field (E_r) has been found to play an important role on the improved plasma confinement in various devices with different configurations, sizes and plasma parameters. The theories predict that the gradient of radial electric field (E_r') or the shear of plasma rotation has a strong influence on the suppression of microinstabilities and is expected to reduce the anomalous transport.[1~7)]

Although a large amount of information for the effects of radial electric field has been accumulated in the tokamak and stellarator experiments, and the theoretical studies, the physical process has not yet been completely understood. The recent observations in tokamaks such as DIII-D [8,9)], CCT [10)], JIPP-TII-U [11)] and JFT-2M [12)], have provided the basis for an increased understanding of the physics associated with electric field, showing that the radial profiles of plasma rotation are different for L-and H-mode equilibria, respectively. Theoretical models have predicted the structural change of radial electric field to explain the transition between two equilibria [2,3,13)], motivating these experimental studies. Extensions have been proposed by several authors.[14~18)] The parallel viscosity associated with shock formation has also revived attractions, and it has been studied in a poloidally rotating tokamak plasma with $M_p \simeq 1$, where M_p is the Mach number of poloidal rotation.[19)] The physics of the generation and structure of the radial electric field is the basis to investigate the role of the electric field on the improved confinement.

In heliotron/torsatron and stellarators, the neoclassical theory suggests that an electric field reduces the helical ripple loss, and consequently improves the energy confinement.[20,21)] The relationship among the electric field, the fluctuations and plasma confienement was studied in the past experiments such as B-3[22)] and JIPP-I[23)], which were the l=3 stellarators. These experiments have led to a qualitative understanding,

but quantitative results have been lacking. The poloidal rotation has been measured by using the intrinsic impurity radiation in the Wendelstein VII-A stellarator(W7-A)[24] and Heliotron-E(H-E)[25] devices. The measurements were limited only near the plasma periphery in these experiments. A progressive measurement with improved time and spatial resolution is necessary to get a data in the whole plasma region. In the Compact Helical System(CHS), the plasma rotation measurement has been carried out recently, and the electric field profile in the whole plasma region is evaluated from both toroidal and poloidal rotation velocities and pressure gradient by using the charge exchange spectroscopy(CXS).[26,27] These recent experimental progresses allow the quantitative analysis on the formation process of radial electric field in helical devices. It has been explained that a large negative electric field was built up by the fast ion orbit loss in the W7-A experiment.[28,29] It should be noted that in the W7-A, the neutral beams are injected almost perpendicular to the magnetic field and a significant loss cone loss of fast ions exists in the plasma. In the CHS experiment, however, neutral beams are injected almost tangentially and the loss cone loss of the injected fast ions is less significant. Comparative study on these configurations would be fruitful in understanding the cooperative mechanism between the radial electric field and loss cone loss.

In the previous papers [30,31], we proposed a theoretical model to determine the radial electric field in the helical systems and applied to the CHS and W7-A experiments. In these studies, however, we discussed the case of perpendicular injection of neutral beams because they are planned to be perpendicularly injected in the CHS experiment although neutral beams are injected almost tangentially at present. It was found from the previous studies that the fast ion orbit loss plays an important role on the radial profile of E_r. Effects of fast ion loss caused by the charge exchange with neutrals has also been discussed. Theoretical results showed that these effects were considerable at

the plasma edge, but the quantitative prediction was not satisfactory, in particular, in the CHS experiment. It should be noted that the theoretical result depends sensitively on the profile of neutral density, for which the accurate experimental data was not given. Therefore, an understanding of the behaviour of neutral hydrogen is essential. Recently, the radial profile of neutral density in the CHS has been evaluated accurately by using two new techniques, namely, a calibrated TV camera with an H_α optical filter and a laser-induced fluorescence method (LIF)[32]. For the theoretical discussions for the effect of neutral particles on the plasma rotation, a non-ambipolar process in the ion particle flux driven by the momentum loss associated with ionization and charge exchange processes has been studied. [33,34] Also, Ohkawa and Miller have proposed to drive a rotation of the surface plasma by injection of heavy ion neutral beams into the edge region of a tokamak plasma.[35] They have pointed out that the radial electric field resulting from this injection can produce large poloidal rotation, in which the neutral drag due to charge exchange could be significant, depending upon the neutral density level and its profile near the plasma edge. The improvement on the measurement techniques and the theoretical suggestion discussed above, encourage the study to explain the discrepancy between theoretical predictions and observations in the CHS experiment, which has been discussed in the previous paper.[30]

In this article, we develop a selfconsistent analysis, which determines the electric field and loss of energetic particles simultaneously, by taking account of orbit loss, charge exchange loss and anomalous loss. A flow chart of mutual relations involved in the analysis is sketched in Fig. 1. We apply this analysis to the NBI heated plasma in the CHS. The partition between the ratio of the bulk heating, direct orbit loss, shine through and the charge exchange loss is also evaluated.

§ 2. A Theoretical Model

In order to determine the radial electric field E_r (r) in the stationary state, we apply the following ambipolarity equation

$$\Gamma^e_{NC} = \Gamma^i_{NC} + \Gamma^i_{lc} + \Gamma^i_{cx} + \Gamma^i_{ano} \tag{1}$$

where the suffix NC indicates the neoclassical contribution, lc for loss cone loss, cx for the charge exchange loss, and ano for the anomalous loss, respectively. The superscripts e and i denote electrons and ions, respectively.

The expression of neoclassical transport we empoly here is quoted from ref.[20]. Analytic formulas are also required to combine the analysis on loss cone under the influence of radial electric field with transport calculation. The analytic formula [36] and numerical analysis [37] based on the theory of J-invariance have been discussed to evaluate the loss regions in both velocity and configuration spaces in the presence of E_r. In these references, we derived a simple analytic expression, which describes the relation between the radial electric field and the minimum energies of the deeply trapped particles and the barely trapped particles entering the loss cone.

We here define the loss cone by the condition that the particles starting from $r = r, \theta = 0$ (or $\theta = \pi$) reaches to r= b at some poloidal angle (b $\geq$ a; a is the minor radius). The loss cone boundary r_* is defined by the condition that particles generated at the radius $r > r_*$ enter the loss cone and those bone in the region $r < r_*$ do not. In case of the negative radial electric field, which is realized generally in the NBI heated plasmas, whether the ion loss cone appears in the inner side of the torus ($\theta = \pi$) or in the outer side of the torus ($\theta = 0$), depends on the magnitude of electric field. We choose a model magnetic field with one helical harmonic as

$$B = B_0[1 - \varepsilon_t(r)\cos\theta - \varepsilon_h(r)\cos(\ell\theta - m\phi)], \tag{2}$$

where $\epsilon_t(r)$ and $\epsilon_h(r)$ represent the toroidal and helical ripples, respectively. Also, we assume that the static potential is constant on the magnetic surface and is given as $\phi(r) = \phi_0 f(r)$. Function f(r) is a monotonic function of r and satisfies f(0) = 0 and f(a) = 1. If the radial electric field is weak, we have the loss boundary[36)]

$$\phi_0 = \phi_1, \tag{3}$$

with

$$\frac{e\Phi_1}{\varepsilon_{ha}\mu B_0} = \frac{(1+\rho-2\kappa_1^2\rho)(1-\rho)-\varepsilon(1+\rho)}{1-f(\rho)} \tag{4}$$

where $\rho = r_*/a, \epsilon = \epsilon_t(a)/\epsilon_{ha}$ with $\epsilon_{ha} = \epsilon_h(a)$ and $\kappa_1 = \kappa(\theta = \pi)$ in which κ^2 is given as

$$\kappa^2 = \frac{\mathcal{W}-\mu B_0(1-\varepsilon_t\cos\theta-\varepsilon_h)-q\Phi}{2\varepsilon_h\mu B_0} \tag{5}$$

On the other hand, if the electric field is so strong that the $E \times B$ rotation reverses the direction of the poloidal drift, we have the loss cone boundary,

$$\phi_0 = \phi_2 \tag{6}$$

where

$$\frac{e\Phi_2}{\varepsilon_{ha}\mu B_0} = \frac{(1-\rho+2\kappa_1^2\rho)(1+\rho)+\varepsilon(1-\rho)}{1-f(\rho)} \tag{7}$$

Combining eqs. (3) and (6), we obtain the loss region for trapped particles as $\phi_1 < \phi_0 < \phi_2$. It is noted that the loss cone boundary for the particles that experience the transition between helically trapped and transit orbits is determined approximately by the relation $\kappa_1^2 = 1$ on the midplane.

Typical examples of the loss cone boundary for helically trapped particles, which are described by eqs.(3) and (6), are illustrated in Figs.2(a) and 2(b). The loss cone boundary for deeply trapped particles is plotted in Fig. 2(a) for two cases, namely, the parabolic potential case with $\phi(\rho) = \phi_0\rho^2$ (solid curves) and a non-parabolic case with

$\phi(\rho) = \phi_0 f(\rho)$ (dotted line), where $f(\rho)$ is the selfconsistent solution of eq. (1). For a negative potential ($E_r > 0$), the loss cone region exists at the outside of torus and decreases as the potential increases. On the other hand, the loss region shifts towards the magnetic axis as the potential increases in case of $\phi > 0 (E_r < 0)$. The loss region spreads over the whole region, namely, at both inside and outside of the torus in some range of negative electric field

$$1 - \varepsilon/2 < e\phi/\varepsilon_{ha}\mathbb{W} < 1 + \varepsilon/2 \tag{8}$$

indicating that the condition of helical resonance is satisfied ($\omega_{E\times B} + \omega_{\nabla B} \simeq 0$). The shaded region in Fig.2(a) represents this loss region caused by helical resonance. Further increase of negative electric field ($E_r < 0$) tends to localize the loss region only inside of the torus. These results are compared to the case of W7-A stellarator. As was discussed in ref.[31], the loss cone exists at the inside of the torus for the level of negative electric field ($E_r \simeq$ - 450 V/cm), observed in the NBI heated plasma in the W7-A experiment. We note that the loss region exists at the outside in the CHS experiment because E_r is negative but relatively weak ($E_r \simeq -(60 \sim 120)$ V/cm at $\rho \simeq 0.7$). Figure 2(b) shows the loss boundary for barely trapped particles ($\kappa_1^2 = 1$) together with that for deeply trapped particles, in the outside of the torus. Comparison between parabolic and non-parabolic potential cases has also been made in Fig. 2(b). It is noted that the loss region is much wider, i.e., closer to the magnetic axis, for the barely trapped particles.

Let us next consider the radial current (see, the second term in eq.(1)) associated with the loss cone loss. In the following discussions, we consider the case of perpendicular neutral beam injection and for simplicity, we choose a model of injected beam, such that the birth profile is limited on the equatorial plane and the radius of the beam channel is neglected. The power flux P(x) is the injection power across the surface x

$= r\cos\theta$. Under this simplified situation, we have derived a form of the radial current associated with the loss cone in a previous article[30] as

$$\Gamma_{lc}(r) = \frac{P(r)-P(r_*)}{4\pi^2 R r W_b} \tag{9}$$

where the suffix lc indicates the loss cone. It is noted that in case of the W7-A, eq. (9) reduces to the expression in ref.[31] if r and r_* are replaced by -r and $-r_*$, because the loss region in the W7-A exists at the inside of the torus while it exists at the outside in case of the CHS experiment. Figure 3 illustrates the drift orbit, the loss cone boundary r_*, and the birth profile of fast ions, S_i(x), schematically. The particle source which is born in the region$[r_*, r]$ contributes to the radial current by the loss cone at r = r. Based on a thin pencil beam model of the injected fast neutral particles, we calculate the birth profile. This simplification allows us to use

$$P(x)/P(a) = \exp\{-\int_x^a \xi(x)(du/dx)dx\} \tag{10}$$

where the integral is taken along the path u, $x = u\cos\theta_{inj}, \theta_{inj}$ is the injection angle of the neutral beam with respect to the magnetic axis and the rate of the ionization ξ is approximated as

$$\xi(x) = n_e < \sigma > \tag{11}$$

where σ is the charge-exchange cross section, which can be approximately given as[38]

$$< \sigma > = \frac{0.6937 \times 10^{-18}(1 - 0.155\ log_{10}E_b)^2}{1 + 0.1112 \times 10^{-14}E_b^{3.3}}[m^2], \tag{12}$$

In eq.(1), the form of the current driven by the charge exchange loss is given as[30,31]

$$\Gamma_{cx} = (c/eB_p)M_f n_f n_0 <\sigma v_b> v_{ft} \tag{13}$$

where B_p is the poloidal magnetic field, M_f is the mass of fast ions, n_0 is the neutral particle density, n_f is the fast particle density, v_b is the beam velocity $\sqrt{2W_b/M_f}, v_{ft}$

is the toroidal velocity of the fast ions, and σ is given by eq.(12). We note that eq.(13) is essentially the same as that by Shaing et al. by replacing the contribution from the fast ions into bulk ions.(see, eq.(6) in ref.[34])

As for the anomalous ion flux in eq.(1) is concerned, the form of Γ_{ano} is chosen, which has the same dependence as the so-called Alcator scaling of anomalous transport in the following forms

$$\Gamma^{i}_{ano} = -\alpha_A(\partial n/\partial r)/n \tag{14}$$

$$q^{i}_{ano} = -\alpha_A\beta_A\partial T_i/\partial r + 1.5\alpha_A T_i(\partial n/\partial r)/n \tag{15}$$

where the coefficients α_A and β_A are the parameters, describing the magnitude of the bipolar part of the anomalous ion transport. q^i_{ano} illustrates the energy flux associated with this process.

We here briefly explain the numerical method of calculation how to determine the radial electric field and the loss rates simultaneously. It is noted that the solution of eq.(1), $E_r(r)$, is a functional of the parameter r_*, because the loss cone current eq.(9) depends on the choice of r_*. If we obtain the solution $E_r(r_j)$, which is the value of E_r at $r = r_j$, we can evaluate approximately the potential from the relation

$$\phi(a) - \phi(r_*) = -\sum_{j=k}^{N} E_r(r_j)(r_j - r_{j-1}) \tag{16}$$

where $r_* = r_k$ and $r_N = a$. Thus, the radial electric field $E_r(r)$ and the eigenvalue r_* are determined to satisfy eq.(1) or eq.(16) and eq.(4) or eq.(7), consistently.

Once the radial electric field and the loss cone boundary are determined, we can calculate the power partition. It is noted that the partition among the shine-through, direct orbit loss, charge exchange loss, and bulk heating is given by the following ratios as

$$\eta_{st} = P(-a)/P(a) \tag{17}$$

$$\eta_{ol} = [P(a)-P(r_*)]/P(a) \tag{18}$$

$$\eta_{cx} = \int_{-a}^{r_*} \{\nu_{cx}/(\nu_{heat}+\nu_{cx})\}p(r)dr \tag{19}$$

$$\eta_{bh} = \int_{-a}^{r_*} \{\nu_{heat}/(\nu_{heat}+\nu_{cx})\}p(r)dr \tag{20}$$

where suffix st, ol, cx and bh denote the shine-through, orbit loss, charge exchange, and bulk heating, respectively. In these equations, P(r) is given by eq.(10), $\nu_{heat} = (m_e/m_i)\nu_{ei}, \nu_{cx} \simeq n_0(r) < \sigma > v_{fast}$ and $p(r) = \xi(r)I(r)$, where I(r) is defined as P(r)/P(a). Here, $m_e(m_i)$ is the mass of electrons(ions) and ν_{ei} is the electron-ion collision frequency. The summation of eq.(19) and eq.(20) yields

$$\eta_{cx} + \eta_{bh} = [P(r_*)-P(-a)]/P(a) \tag{21}$$

Therefore, these ratios(17) - (21) satisfy the relation

$$\eta_{st} + \eta_{ol} + \eta_{cx} + \eta_{bh} = 1 \tag{22}$$

which is the energy conservation relation.

§3. Application to the NBI Heated Plasma in CHS

The CHS device is a torsatron/heliotron configuration (l = 2, m = 8) with a major radius of 100 cm and an average minor radius of 20 cm. The toroidal magnetic field is 1T and 2T operation has been available. As is mentioned partly in §1, the electron temperature and density profile, $T_e(r)$ and $n_e(r)$, are measured with Thomson scattering. The ion temperature and poloidal as well as toroidal rotation velocity profiles,

$T_i(r)$, U_θ and U_ϕ are measured by the CXS. Recently, the limited amount of the data of the neutral density profile can be also measured by a laser-induced fluorescence technique. For the NBI discharges in CHS, as was studied in the previous papers[26], the toroidal rotation is damped at r>0.3a but the poloidal rotation has a strong shear near the plasma edge, which comes from the inhomogeneity of the radial electric field. This tendency is remarkable in case of a high density NBI experiment.

3.1 Effect of Fast Ion Orbit Loss

We now study the effect of fast ion orbit loss on the radial electric field, E_r for given profiles of plasma density and temperatures of the NBI heated plasma in the CHS device.[26,30] Here, we assume almost perpendicular neutral beam injection instead of the tangential injection. As a first step, the contribution of neutral particles is neglected (This effect will be discussed later). Two typical cases, namely, the low and high density NBI discharges are studied to understand the dependence of collisionality on the radial profile of E_r, which has been studied experimentally. Figure 4 shows the sample distributions of density and temperature for low(A) and high(B) density cases. The following fitting curves for bulk plasma parameters are assumed as [30]

$$n(\rho) = (n(0)-n_s)\frac{(1-\rho^{\alpha_2})}{\gamma}[1-(1-\gamma)(1-\rho^{\alpha_2})^{\beta_2-1}]+n_s, \tag{23}$$

$$T_e(\rho) = (T_e(0)-T_{es})(1-\rho^{\alpha_3})^{\beta_3}+T_{es}, \tag{24}$$

$$T_i(\rho) = (T_i(0)-T_{is})(1-\rho^{\alpha_4})^{\beta_4}+T_{is}, \tag{25}$$

where ρ is the normalized radius r/a, and the indices (α_k, β_k) are constant (k=2-4). The coefficient γ is introduced to fit the hollow profile, and is given by $\gamma = 1 - \beta_2^{-1}[1 - \rho_m^{\alpha_2}]^{(1-\beta_2)}$, where ρ_m is the minor radius corresponding to the maximum of the density. Also, n_s and T_s represent the values at the plasma edge. For the present analysis, we choose the shaping parameters, so as to reproduce the experimental result, which are $\alpha_2 = 3.86(6.4975), \beta_2 = 1.1(20.5959), \alpha_3 = 1.5(1.8), \beta_3 = 0.9152(1.0612), \alpha_4 = 1.5(1.5), \beta_4 = 1.165(1.000), n_{eo} = 1.804(5.563) \times 10^{19}/m^3, n_s = 1.043(0.8831) \times 10^{18}/m^3, T_{eo} = 329.9(195.02)$ eV, $T_{es} = 26.65(5.00)$ eV, $T_{io} = 203.1(178.27)$ eV, $T_{is} = 26.70(5.00)$ eV for the low (high) density discharges, respectively. The injection power is taken to be 1 MW.

We are now in position to determine the loss boundary and the radial electric field self-consistently. In the following studies we restrict the discussions to the loss cone boundary for deeply trapped particles with $v = v_\perp$. (The assumption of the parabolic potential profile, which simplifies the analysis, gives the sufficiently accurate results. For the range of the present study, we confirmed the weak dependence on the choice of the potential profile in the range of E_r observed in the CHS, which is seen from Fig.2). We note that the injection energy in these experiments is $W_b \simeq 36$ keV but substantial part of the injection power is carried by the particles with the energy of $W_b/2$ or $W_b/3$ in CHS and W7-A experiments. Therefore, we usually take W_b as 18 keV(half of the nominal injection energy is chosen as an average). Figure 5 shows the energy dependence of the loss cone boundary for the low (A) and high (B) density cases. The loss cone boundary in case of $\phi = 0$ is given by, $\rho_* = 1 - \epsilon \simeq 0.33$, which can be derived by putting $\kappa_1^2 = 0, \phi_1 = 0$ and $f(\rho) = \rho^2$ in eq.(4), is also shown by dotted line. The loss cone boundary shifts toward the magnetic axis as the injection energy is decreased. This is due to the fact that the loss region moves toward the magnetic axis and the

radial electric field near the plasma edge as well as the potential difference between the plasma surface and the loss boundary $\phi(a) - \phi(r_*)$, is consequently increased as W_b decreases (see, eq.(9)).

The radial profile of the power flux and the normalized loss cone current are shown in Fig. 6 for low(A) and high(B) density discharges in the cases of(a) $W_b = 36$ keV, (b) 18 keV and (c) 12 keV. The ratio of the power partition is shown in Fig. 7 for the low (A) and high (B) density cases. For the low density case, the bulk heating(η_{bh}) is effective but is still less than 30 % in the low injection energy ($W_b = 12$ keV). The bulk heating is not effective and the shine-through(η_{st}) is extremely large (more than 80%) in case of the high energy ($W_b = 36$ keV) (Note that the perpendicular injection is assumed). On the other hand, for the high density case, the shine through reduces but the orbit loss (η_{ol}) increases up to about 40 % due to the enhanced radial electric field in case of the intermediate energy ($W_b = 18$ keV). Lower injection energy ($W_b =$ 12 keV) reduces the shine through and increases the orbit loss (about 50 %). However, the bulk heating rate decreases again gradually. Therefore, there is the optimum of the injection energy in an energy range between 18 keV and 12 keV, which gives an effective bulk heating ($36 \sim 37\%$). By determining the loss boundary r_* self-consistenly on the basis of eqs. (1), (4), (9) and (16), we obtain the radial profiles of the electric field, which are shown in Fig. 8(A) for the low density and in Fig. 8(B) for the high density, respectively. In Fig. 8(A), the curves(a) to (c) represent the radial profiles of E_r for the cases ; (a) without orbit loss, (b) with orbit loss ($W_b = 18$ keV) and (c) $W_b = 12$ keV. In Fig. 7(B), the radial profiles of E_r for the case of no orbit loss, $W_b = 36$ keV, 18 keV and 12 keV are shown by the curves (a) to (d), respectively. Figure 8 shows that the fast ion loss flux caused by the loss cone makes the electric field more negative but the influence of the orbit loss appears only in the plasma edge with r > 0.9a although

the loss cone exists in the region with $r > r_*(r_* \sim 0.3a)$. As was shown in the previous paper[26,30], the experimental observation indicates that the negative electric field is - 60 V/cm for the low density and - 120 V/cm for the high density at $r \simeq (0.6 \sim 0.8)a$, which are four or five times as large as the theoretical results as shown in Fig. 8. Moreover, the fast ion orbit loss no longer plays an important role on the enhancement of radial electric field at this region because the effect in case of the tangential injection of neutral beams in the CHS experiment may be weaker than the case of perpendicular injection under consideration. Therefore, some other ion loss process, which is several times as large as the neoclassical loss, is necessary in the region of 0.5 a < r < 0.8a to explain the discrepancy between theoretical results and experimental observations.

3.2 Effect of Neutral Particles

We study the effect of charge exchange loss of fast ions with neutrals on the radial electric field and the partition of beam power. Recently, the neutral hydrogen profile in the core plasma region and the toroidal/poloidal distributions in the recycling area near the inner wall are measured in the CHS experiment by using a calibrated TV camera and a laser-induced fluorescence method.[32] In the following calculations, we use these experimental results for neutral density as a reference parameter in addition to the data as shown in Fig. 4.

To examine the effect of the neutral particles on the radial electric field, we first neglect the effect of fast ion orbit loss, and choose a model distribution for fast particles and neutral particles as

$$n_0(\rho) = n_{0s} \exp[-\alpha_0(1-\rho)^2], \tag{26}$$

and

$$n_f(\rho) = n_{f0} \exp[-\alpha_1 \rho^2], \tag{27}$$

where n_{f0} is the fast ion density at the center, n_{0s} is the neutral particle density at the plasma edge. Parameters α_f and α_0 are assumed to be constant. As a model case, we take the shaping parameters as $\alpha_f = 2$ and $\alpha_0 = 10$, modelling the broad fast ion profile and reproducing the profile of neutral density as shown in ref.[32]. Figure 9 illustrates the radial profile of the net particle flux, $\Gamma^e = \Gamma^i$, for the low density case (A) and the high density case(B). We have chosen the parameter $n_{fo} = 10^{18}/m^3$. Neutral particle density is varied as (a) $n_{os} = 0, (b)4 \times 10^{16}/m^3, (c)8 \times 10^{16}/m^3, (d)2 \times 10^{17}/m^3$ and $(e)5 \times 10^{17}/m^3$ in case of low density (A), and also (a)$n_{os} = 0$, (b) $1.5 \times 10^{17}/m^3$, (c) $4 \times 10^{17}/m^3$, (d) $8.0 \times 10^{17}/m^3$, and (e) $1.5 \times 10^{18}/m^3$ in case of high density (B). The charge exchange loss fluxes, Γ_{cx} in eq.(1) are also plotted separately by dotted lines in Figs.9(A) and 9(B) to understand the contribution from the neutral particles. Figure 10 shows the radial electric field for the low density (A) and the high density(B) in the presence of neutral particle contributions. Open and closed data points in Figs. 10(A) and 10(B) are the experimental values, which are quoted from ref.[26]. As was shown in Figs. 10, the charge exchange loss of fast ions can be effective in enhancing the electric field, and the theoretical results approach to the experimental observations as the neutral density increases up to level of $10^{17}/m^3$ for the low density and $10^{18}/m^3$ for the high density.

It is often discussed that the enhanced electric field can reduce the energy and particle losses. We study the influence of the energetic particle loss on the neoclassical flux of bulk particles. As is seen from Fig. 9 and Fig. 10, the particle flux becomes larger although the energetic particle loss caused by the charge exchange process makes the radial electric field more negative. By this mechanism, the net particle flux increases

due to the fast particle loss. Thus, the increment of the particle flux gives rise to somehow reduction of the particle confinement. The neoclassical energy flux of ions is shown in Fig.11(A) for low density and in Fig.11(B) for high density. The neoclassical energy fluxes in case of $E_r = 0$ and $E_r \neq 0$ are also plotted. We see that the ion energy flux decreases due to the enhancement of E_r caused by the fast particle effect. The electron energy flux, on the other hand, increases by increasing negative radial electric field, which is not shown in this paper.

We next evaluate the partition among the shine through (η_{st}), cx loss of fast particles (η_{cx}) and bulk heating (η_{bh}). The partition rates versus the neutral density at the edge, n_{os} is shown in Fig. 12(A) for low density and in Fig.12(B) for high density. The radial electric fields at $\rho = 0.7$ and 0.9 are also plotted in these figures. For the low density case, the shine through is 57 % and the charge exchange loss increases but consequently, the bulk heating rate decreases(19 %) when n_{os} changes from $2 \times 10^{16}/m^3$ up to $5 \times 10^{17}/m^3$. For the high density case, the shine through is 24% and η_{cx} increases but η_{bh} decreases remarkably(33 %) as n_{os} changes from $4 \times 10^{17}/m^3$ up to $8 \times 10^{17}/m^3$. Therefore, it is important to discuss the trade off concerning on the energy balance. We define the reduction of the neoclassical ion energy flux as

$$\Delta q_1^i = q_{NC}^i - q_{NC+orbit}^i \tag{28}$$

and

$$\Delta q_2^i = q_{NC}^i - q_{NC+cx}^i \tag{29}$$

which are caused by the enhancement of the radial electric field by the orbit loss and charge exchange loss of fast ions, respectively. Also we can evaluate the loss power associated with these fast ion loss processes by using the relations of $P_{ol-Loss} = \eta_{ol} \cdot P_{in}$ and $P_{cx-Loss} = \eta_{cx} \cdot P_{in}$ where P_{in} is the injection power, η_{ol} and η_{cx} are shown in Fig. 12. Figure 13 shows the ratio between the reduction of ion energy flux and loss power

for typical magnetic surfaces ($\rho = 0.7, 0.8$ and 0.9). Here, (A) and (B) represent the results for the low and high density cases, respectively. In these calculations, we take $W_b = 18keV$ and $P_{in} = 1MW$. The ratio, $\Delta q/P_{ol-Loss}$ remains at the 1 % level and the ratio, $\Delta q/P_{cx-Loss}$ increases up to 10 %(20%) for low(high) density case as the neutral density increases. In all cases, however, the power loss of fast ions is greater than the reduction of the bulk ion loss by a factor of several tens to 100.

3.3 Effect of Orbit Loss plus Charge Exchange Loss

Charge exchange loss can affect the loss cone boundary by changing the radial electric field. These two losses can interact with each other. We therefore determine self-consistently the radial electric field under the influence of both the orbit loss and charge exchange loss of fast ions. Figure 14 shows the loss cone boundary and the potential difference between the surface and loss cone boundary $\phi(a) - \phi(r_*)$ for the low density(A) and high density(B), as a function of the neutral particle density. The potential difference, $\phi(a) - \phi(\rho_*)$ increases and the loss cone boundary is shifted inwardly as the neutral density increases. This tendency is remarkable in case of high density. This is in contrast to the case of W7-A stellarator. It should be noted that the enhanced radial electric field caused by the loss of fast ions is effective in narrowing the loss cone in the W7-A experiment.[29)]

The ratio of the power partition versus the neutral density at the edge, n_{os} is shown in Figs. 15(A) for low density and in Fig. 15(B) for high density. The radial electric fields at $\rho = 0.7$ and 0.9 are also plotted. As is seen from Figs. 15, the radial electric field is slightly enhanced by the orbit loss. However, the bulk heating efficiency becomes worse. This clearly shows that the further enhancement of the radial electric field by

using the orbit loss of fast ions in addition to the charge exchange process is not useful so long as one considers the neoclassical energy loss.

3.4 Effects of Anomalous Particle Loss

We finally study the effect of the bipolar part of the anomalous particle loss on the radial electric field on the basis of eqs.(1) and (14). Recently, much effort has been made to evaluate the local transport coefficients experimentally in the CHS for the neutral beam heated plasmas. As was mentioned in the introduction, the local particle transport is examined for neutral beam heated plasma in CHS based on new experimental observations of neutral hydrogen density.[39] These observations show that the plasma density is $(1.5 \sim 2.5) \times 10^{19}/m^3$, the total particle flux is $(2 \sim 3) \times 10^{20}/s$ and the diffusion coefficient D is $(0.3 \sim 0.4)[m^2/s]$ at $\rho \simeq 0.7$. Using these experimental results, we assume the upper bound of the bipolar part of the anomalous coefficient as $\alpha_A \simeq (5 \sim 10) \times 10^{18}$. We use it in eq.(14) in the following calculations in order to study the influence of the possible bipolar anomalous flux. The other parameters are the same as that in Fig. 15. Figure 16 shows the radial profile of electric field for different values of α_A; $(a)\alpha_A = 0, (b)\alpha_A = 5\times10^{18}$, and $(c)\alpha_A = 1.0\times10^{19}$ with $\beta_A = 2.0$ and n_{0s} fixed. The results for low density and high density are shown in Fig. 16(A) and Fig.16(B), respectively. Open and closed data points in Figs. 16(A) and 16(B) are the experimental values, which are quoted again from ref.[26] for comparison. The inclusion of anomalous particle loss in addition to the orbit loss and charge exchange loss further enhances the radial electric field at the plasma edge. We note that small reduction of E_r for $\rho \leq 0.8$ in case of low density is due to the hollow profile of the density as was shown in Fig. 4.

§4. Summary and Discussion

In this paper, we have developed a selfconsistent analysis in determining the radial electric field and loss cone in torsatron/heliotron configurations under the influence of nonclassical ion losses. We examined the effects on the radial electric field, which come from the loss cone loss of fast ions, the loss of fast ions through charge exchange with neutrals, and an anomalous loss. Analysis was applied to the NBI heated plasma in the CHS device. Comparison was made between the theoretical results and experimental observations.

The increased ion particle losses caused by the orbit loss and charge exchange loss of fast ions make the radial electric field deeper compared to the prediction of the neoclassical theory. The fast ion orbit loss gave a more negative E_r but its effect was prominent only near the plasma edge with $r > 0.9a$(see, Fig. 8). This result confirms the previous calculation in which the loss cone boundary was kept constant and not solved consistently. The experimental observations in the NBI heated plasma of the CHS experiment indicated that the radial electric field were -60 V/cm(-120 V/cm) at $r \simeq (0.6 \sim 0.8)a$ in case of low(high) density operation, which were several times as large as the theoretical results. In this paper, we considered the effect of fast ion orbit loss in case of perpendicular injection of neutral beams instead of the tangential injection, which has been carried out in the CHS experiment. Since the effect of orbit loss in case of tangential injection may be weaker than in case of perpendicular injection, we conclude that the loss cone loss of fast ions is less significant on the enhancement of radial electric field around $r \simeq (0.6 \sim 0.8)a$ in the present experiment.

We also studied the effect of charge exchange loss of fast ions with neutrals on the radial electric field and the partition of beam power. It turned out that the charge exchange loss of fast ions can be effective in making the electric field more negative,

and the theoretical results approach to the experimental observations if the theoretical choice of the neutral density at the plasma edge increases up to the level of $10^{17}/m^3$ for the high density case(see, Fig. 10). In these studies, we used the experimental result for neutral density[32] as a reference parameter because the data for the density, ion and electron temperatures of bulk plasma, neutral density, toroidal and poloidal rotations have not obtained simultaneously. It should be noted that the characteristic plasma parameters as was shown in Fig. 4 have been obtained in the NBI experiment, where the position of magnetic axis is 97 cm, and the data for neutral density have been obtained in case of the experiment with $R_{axis} = 92$ cm. We note that the density profile becomes a more peaked profile as the magnetic axis shifted inwardly. The further progress in accumulating the simultaneous experimental data would provide a test of the validity of the present analysis. Charge exchange loss of fast ions with neutrals can affect the loss cone boundary by changing the radial electric field, and consequently, these two losses interact with each other.

We have carried out a selfconsistent analysis by taking account of this situation. The partition among the shine through, the direct loss, and the charge exchange loss through changing the radial electric field must be kept in consideration, when the heat load onto the wall is analyzed. From the over all consideration on the energy balance, we studied the enhancement of radial electric field due to both the orbit loss and charge exchange loss of fast ions. Also, we evaluated the loss power associated with these loss processes of fast ions. The radial electric field was slightly enhanced by adding the orbit loss to the charge exchange loss. However, the bulk heating efficiency becomes worse. In all cases, moreover, the power loss of fast ions is by a facter of several tens to hundred greater than the reduction of the energy loss of bulk ions through the enhancement of electric field(see, Fig. 13). These results clearly show that the enhancement of E_r,

which is caused by the orbit loss and/or the charge exchange loss is not profitable so long as one considers the neoclassical energy loss.

The particle and energy balance in real experiments are strongly influenced by an anomalous transport. We also investigated the effect of the possible bipolar component of the anomalous loss on the change of radial electric field. The role of the radial electric field on the anomalous transport still needs further investigations experimentally and theoretically, in order to conclude the over all trade-off on the energy balance. In this article, we employed a formula of the loss cone boundary, which is valid to general form of the radial electric field. By using this selfconsistent form for loss cone boundary, we found that the simplified model for the loss cone can give a good approximate solution. Namely, the solution of the radial electiric field can be approximated by the simplification that the loss cone boundary is determined with a simple parabolic model of the static potential. Our result gives a basis to employ the simplified model for future analysis.

Acknowledgements

The authors wish to acknowledge useful disccusions with Dr. K. Ida, Dr. H. Yamada, Dr. K. Matsuoka, Dr. M. Fujiwara, and the CHS group. They are grateful to Dr. H. Iguchi and Dr. S. Morita for stimulating discussions on the experimental data of neutral particles. This work is partly supported by the Grant-in-Aid for Scientific Research of Ministry of Education, Japan.

References

1) H. Sanuki : J. Phys. Soc. Jpn. 52(1983) 511, Phys. Fluids 27(1984) 2500, H. Sanuki and R. D. Ferrano: Phys. Scr. 34(1986)58.

2) S.-I. Itoh, K. Itoh, T. Ohkawa, et al. : in Plasma Physics and Controlled Nuclear Fusion Research 1988, Proc. 12 th Int. Conf. Nice, 1988(IAEA Vienna 1989) Vol. 2, p23.

3) K. C. Shaing, et al. : in Plasma Physics and Controlled Nuclear Fusion Research 1988, Proc. 12 th Int. Conf. Nice, 1988 (IAEA Vienna 1989) Vol. 2, p13.

4) K. C. Shaing, E. C. Crume, Jr., and W. A. Houlberg : Phys. Fluids B2(1990)1492.

5) H. Sugama and M. Wakatani : J. Phys. Soc. Jpn. 58(1989)1128.

6) S.-I. Itoh, H. Sanuki and K. Itoh : J. Phys. Soc. Jpn. 60(1991)1891.

7) G. M. Staebler and R. R. Dominquez : Nucl. Fusion 31(1991)1891.

8) R. J. Groebner et al. : Phys. Rev. Lett. 64(1990)3015.

9) K. H. Burrell et al. : Phys. Fluids B(1990)1405.

10) R. J. Taylor et al. : Phys. Rev. Lett. 63(1989)2365.

11) K. Ida et al. : Nucl. Fusion 31(1991)943.

12) Y. Miura and JFT-2M Group : in 13 th Int. Conf. on Plasma Physics and Controlled Nuclear Fusion Research (IAEA, Washington, 1990) Paper IAEA-CN-53/A-4-2.

13) S.-I. Itoh and K. Itoh : Phys. Rev. Lett. 60(1988)2276.

14) K. C. Shaing and E. C. Crume Jr. : Phys. Rev. Lett. 63(1989)2369.

15) H. Biglari, P. H. Diamond and P. W. Diamond : Phys. Fluids B2 (1990)1.

16) S.-I. Itoh and K. Itoh : J. Phys. Soc. Jpn. 59(1990)3431.

17) A. B. Hassam et al. : Phys. Rev. Lett. 66(1991)309.

18) F. L.Hinton : Phys. Fluids B3 (1991)696.

19) K. C. Shaing, R. D. Hazeltine and H. Sanuki : Phys. Fluids B4(1992)404.

20) L. M. Kovrizhnykh : Nucl. Fusion 24(1984)435.

21) D. E. Hastings, W. A. Houlberg and K. C. Shaing : Nucl. Fusion 25(1985)445.

22) J. G. Gorman and L. H. TH. Rietjents : Phys. Fluids 9(1966)2504.

23) A. Mohri and M. Fujiwara : Nucl. Fusion 14(1974)67.

24) H. Wobig, H. Maassberg, H. Renner, The WVII-A Team : in Plasma Physics and Controlled Nuclear Fusion Research, 1986, Proc. 11th Int. Conf. Kyoto, 1986 (IAEA Vienna 1987) vol. 2, p 369.

25) K. Kondo, H. Zushi, S. Nishimura, et al. : Rev. Sci. Instrum. 59(1988)1533.

26) K. Ida, H. Yamada, H. Iguchi, et al. : Phys. Fluids B3 (1991)515, B4(1991)1360.

27) K. Ida, H. Yamada, H. Iguchi, K. Itoh and CHS Group : Phys. Rev. Lett. 67(1991)58.

28) H. Renner, WVII-A Team, NBI Group, ICF Group: 'Overview on recent WVII-A experimental results', in Proc. 6th International Stellarator/Heliotron Workshop (IAEA Tech Committee Meeting, Kyoto, 1986) Vol. 1, p23.

29) WVII-A Team and NI Team : in Prof. 11th European Conference on Controlled Fusion and Plasma Physics (Aachen, 1983) Vol. 7D Part I, p199.

30) H. Sanuki, K. Itoh, K. Ida and S.-I. Itoh : J. Phys. Soc. Jpn. 60(1991)3698.

31) K. Itoh, H. Sanuki and S.-I. Itoh : (to be published in Nucl. Fusion 32 (1992)).

32) K. Uchino, H. Takenaga, et al. : Research Report of Plasma Engineering Laboratory, Kyushu Univ. No. 274 (1992), to be published in J. Nuclear Materials.

33) T. Ohkawa: Kakuyuugou Kenkyuu 56 (1986)274.

34) K. C. Shaing, W. A. Houlberg and E. C. Crume : Comments Plasma Phys. Controlled Fusion 12(1988)69.

35) T. Ohkawa and R. L. Miller : in 13th Int. Conf. on Plasma Physics and Controlled Nuclear Fusion Research (IAEA, Washinton, 1990) Paper IAEA-CN-53/A-7-11.

36) K. Itoh, H. Sanuki, J. Todoroki, et al. : Phys. Fluids B3 (1991)1294.

37) H. Sanuki, J. Todoroki and T. Kamimura : Phys. Fluids B2(1990)2155.

38) A. C. Riviere : Nucl. Fusion 11 (1971)363.

39) H. Iguchi et al. : to be presented in 1992 Int. Conf. on Plasma Physics and 19th European Conference on Controlled Fusion and Plasma Physics (Innsbruck, Austria).

Figure Captions

Fig. 1 A flow chart of several topics associated with E_r and / or E_r' involved in the present analysis.

Fig. 2 Loss cone boundary for deeply trapped particles (a) for a parabolic potential case (solid curves) and for a non-parabolic case (dotted line). The bounded region by the lower boundary [eq.(3)] and the upper boundary [eq.(6)] represents the loss region. In (a), the shaded region represents the loss region caused by helical resonance. Loss cone boundary for barely trapped particles ($\kappa_1^2 = 1$) together with the result for deeply trapped particle are shown in (b) for parabolic(solid curves) and non-parabolic (dotted lines) potentials. Here we used $W_b = 18$ keV and $\epsilon = \epsilon_{ta}/\epsilon_{ha}$.

Fig. 3 Schematic plot of the drift surface of the fast ions and neutral beam(a). r_* indicates the loss cone boundary. The current across the surface r = r associated with the loss cone is given by the particle source in the region [r_*, r]. Beam power density P, birth profile S and the loss cone current are shown schematically in (b).

Fig. 4 Radial profiles of the density ($n(\rho)$), ion and electron temperatures (T_i, T_e) for the low density(A) and high density (B) NBI discharges in CHS device.

Fig. 5 Dependence of beam energy on the loss cone boundary for deeply trapped particles in low(A) and high(B) density cases. Loss cone boundary in case of $\phi = 0$ is also plotted by dot-dash line.

Fig. 6 Radial profile of the power flux(solid lines) and the normalized loss cone currents(dotted lines) for low(A) and high(B) density discharges in case of (a) $W_b = 36$ keV, (b) 18 keV and 12 keV.

Fig. 7 Dependencel of beam energy on the power partition among shine through (η_{st}), orbit loss (η_{ol}) and bulk heating (η_{bh}) for low(A) and high(B) density cases.

Fig. 8 Radial electric field determined selfconsistetly under the influence of orbit loss for low(A) and high (B) density cases. In (A), the results (a) to (c) represent the radial profile of E_r in case of (a) without orbit loss, (b) with orbit loss ($W_b = 18$ keV) and (c) with orbit loss ($W_b = 12$ keV) for low density case. The radial profiles of E_r in case of (a) $W_b = 0$, (b) $W_b = 36$ keV, (c)$W_b = 18$ keV, and (d) $W_b = 12$ keV are shown in (B) for high density case.

Fig. 9 Radial profiles of net particle flux ($\Gamma^e = \Gamma^i \equiv \Gamma$) versus several values of neutral density at the plasma edge, n_{os} for low(A) and high(B) density cases. In(A), (a) $n_{os} = 0$, (b) $4 \times 10^{16}/m^3$, (c) $8 \times 10^{16}/m^3$, (d) $2 \times 10^{17}/m^3$, and (e) $5.0 \times 10^{17}/m^3$. In (B), (a)$n_{os} = 0$, (b)$1.5 \times 10^{17}/m^3$, (c) $4 \times 10^{17}/m^3$, (d) $8.0 \times 10^{17}/m^3$, and (e) $1.5 \times 10^{18}/m^3$. Charge exchange loss fluxes, Γ_{cx} are also plotted by dotted lines.

Fig.10 Radial electric fields in the presence of neutral particle contribution.(A) and (B) correspond to the low and high density cases. Experimental observations are also shown by open and closed data points, which are quoted from ref.[26]. In (A), (a) $n_{os} = 0$, (b) $4.0 \times 10^{16}/m^3$, (c) $8.0 \times 10^{16}/m^3$, (d) $2.0 \times 10^{17}/m^3$, and (e)$5.0 \times 10^{17}/m^3$. In (B), (a) $n_{os} = 0$, (b) $1.5 \times 10^{17}/m^3$, (c) $4.0 \times 10^{17}/m^3$, (d) $8.0 \times 10^{17}/m^3$, and (e)$1.5 \times 10^{18}/m^3$.

Fig.11 Radial profiles of neoclassical energy flux of ions versus neutral particle densities for low (A) and high (B) density cases. In (A), (a) $n_{os} = 4.0 \times 10^{16}/m^3$, (b) $8.0 \times 10^{16}/m^3$, (c) $1.5 \times 10^{17}/m^3$, and (d) $2.0 \times 10^{17}/m^3$. In(B), (a) $n_{os} = 8.0 \times 10^{16} m^3$, (b) $1.5 \times 10^{17}/m^3$, (c) $2.5 \times 10^{17}/m^3$, and (d) $4.0 \times 10^{17}/m^3$. The neoclassical energy fluxes in case of $E_r = 0$ and $E_r \neq 0$ without neutral particle contribution are also plotted.

Fig.12 Partition rates among the shine through (η_{st}), charge exchange loss (η_{cx}) and bulk heating (η_{bh}) versus the neutral density, n_{os} for low (A) and high (B) densities. Radial electric fields at $\rho = 0.7$ and 0.9 are also shown.

Fig.13 Dependence of neutral density on the ratio between the reduction of ion energy flux and loss power for typical magnetic surfaces ($\rho = 0.7, 0.8$ and 0.9). Here, $W_b = 18$ keV and $P_{in} = 1$MW. (A) and (B) correspond to the low and high denstiy cases. The ratio between the reduction of ion energy flux and loss power caused by the orbit loss is also plotted.

Fig.14 Loss cone boundary and potential difference between the plasma surface and loss cone boundary, $\Phi(a) - \Phi(r_*)$ for low (A) and high (B) densities as a function of neutral particle density.

Fig.15 Partition rates among the shine through (η_{st}), orbit loss (η_{os}), charge exchange loss (η_{cx}) and bulk heating (η_{bh}) versus the neutral density n_{os}. Here, both orbit loss and charge exchange loss are taken into account. (A) and (B) represent the results of low and high density cases. Radial electric fields at $\rho = 0.7$ and 0.9 are also shown.

Fig.16 Radial profile of E_r for several values of α_A; $(a)\alpha_A = 0, (b)5\times10^{18}, (c)1.0\times 10^{19}$ with $\beta_A = 2.0$ fixed and $n_{0s} = 5.0 \times 10^{17}/m^3$ in (A) and $1.5 \times 10^{18}/m^3$ in (B) are used. The results for low density and high density are shown in (A) and (B), respectively. Open and closed data points are the experimental results, which are quoted from ref.[26].

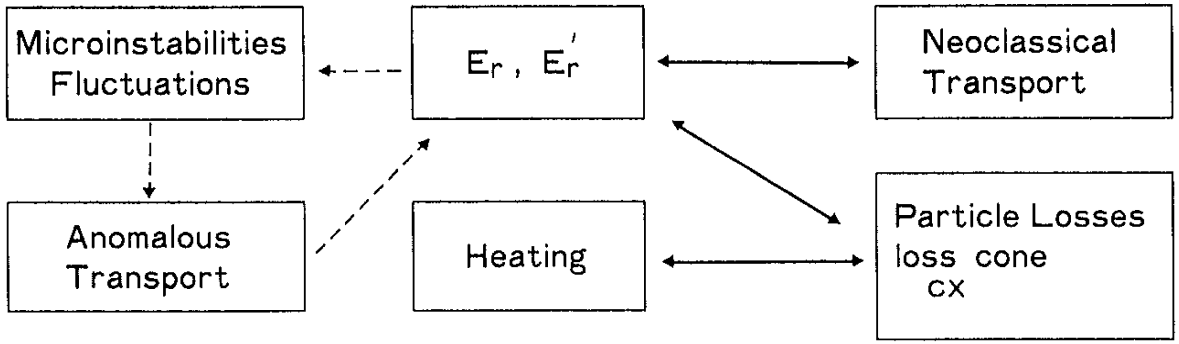
Microinstabilities
Fluctuations
E_r , E_r'
Neoclassical
Transport
Anomalous
Transport
Heating
Particle Losses
loss cone
cx

F i g . 1

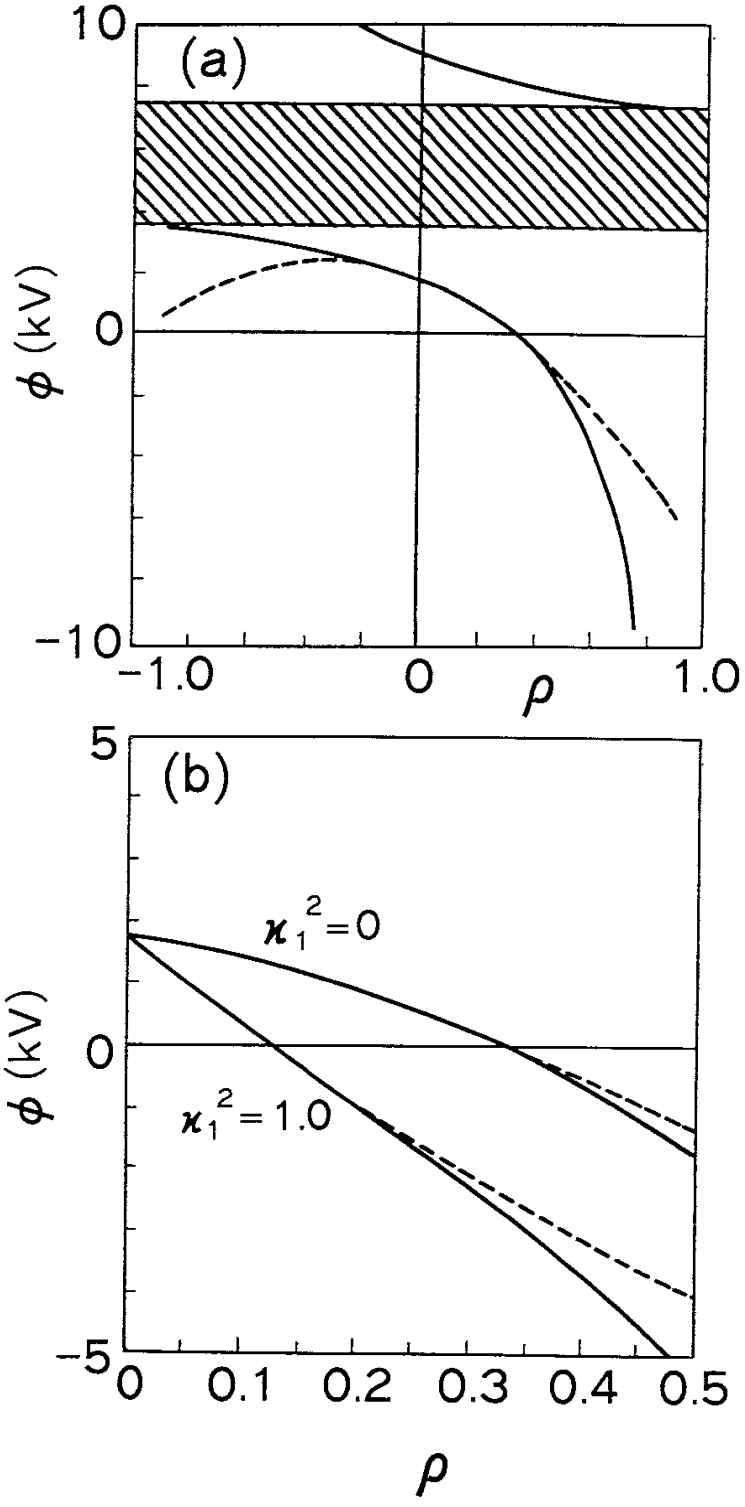
10
(a)
0
−10
φ (kV)
−1.0
0
ρ
1.0
5
(b)
$\varkappa_1^2=0$
$\varkappa_1^2=1.0$
0
−5
φ (kV)
0
0.1
0.2
0.3
0.4
0.5
ρ

Fig. 2

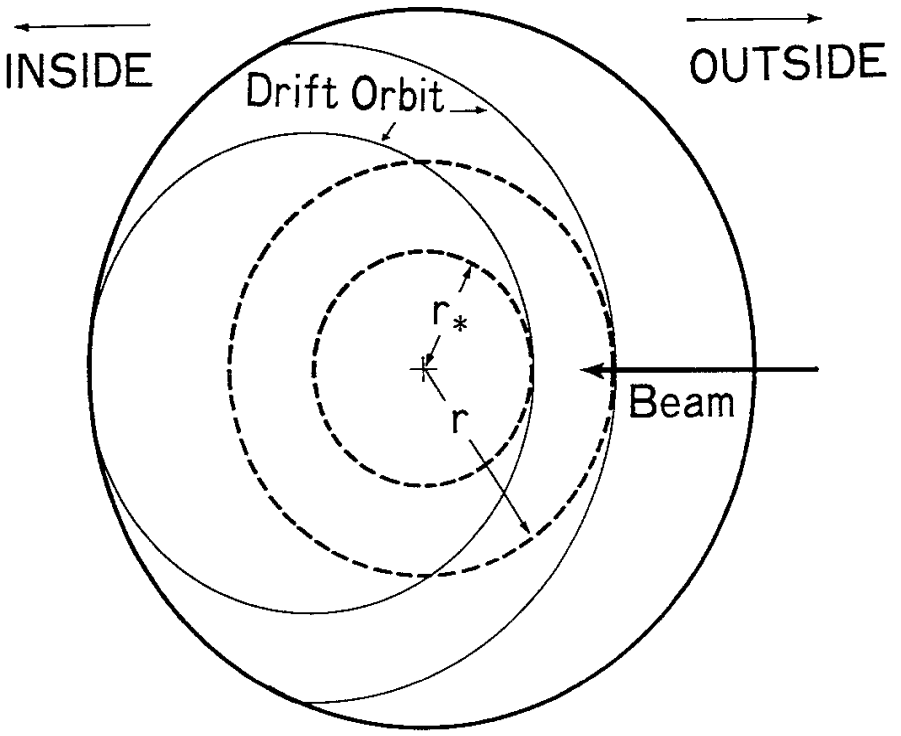

(a)

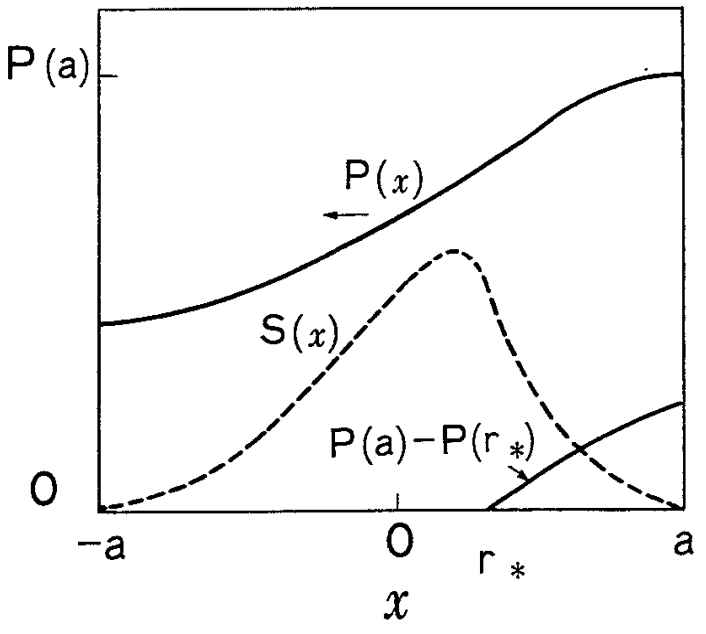

(b)

Fig. 3

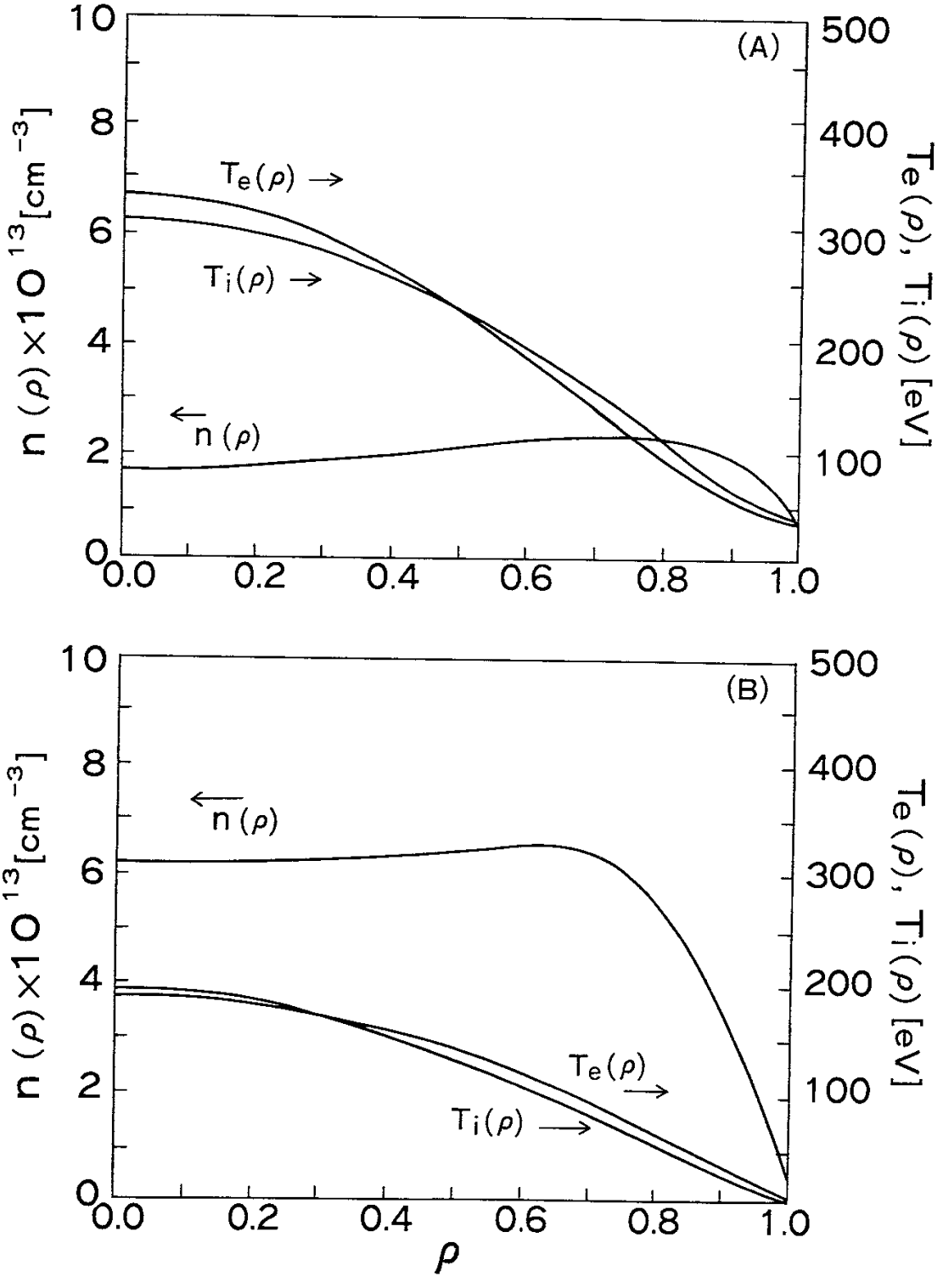
(A)
$T_e(\rho)$ →
$T_i(\rho)$ →
← $\overline{n}(\rho)$
$n(\rho) \times 10^{13}$[cm^{-3}]
$T_e(\rho)$, $T_i(\rho)$ [eV]
(B)
← $\overline{n}(\rho)$
$T_e(\rho)$ →
$T_i(\rho)$ →
ρ

Fig. 4

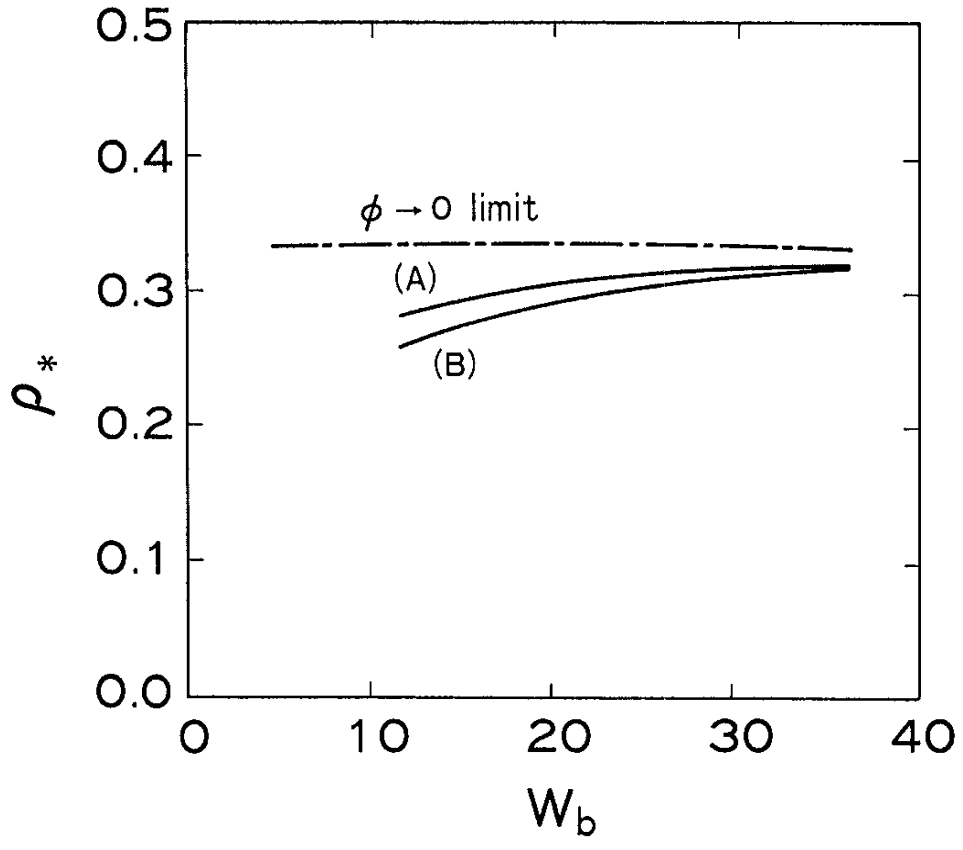

F i g . 5

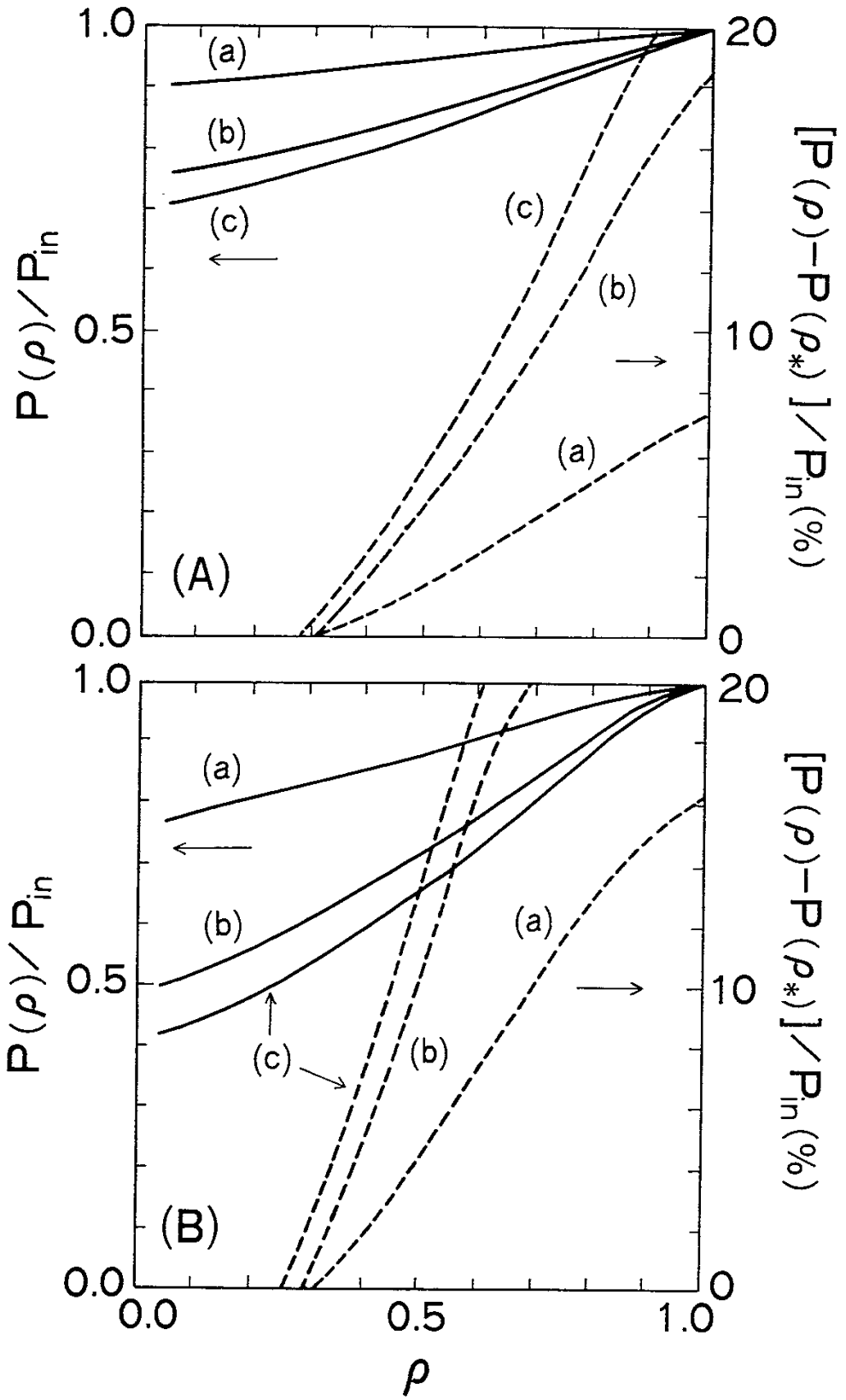

Fig. 6

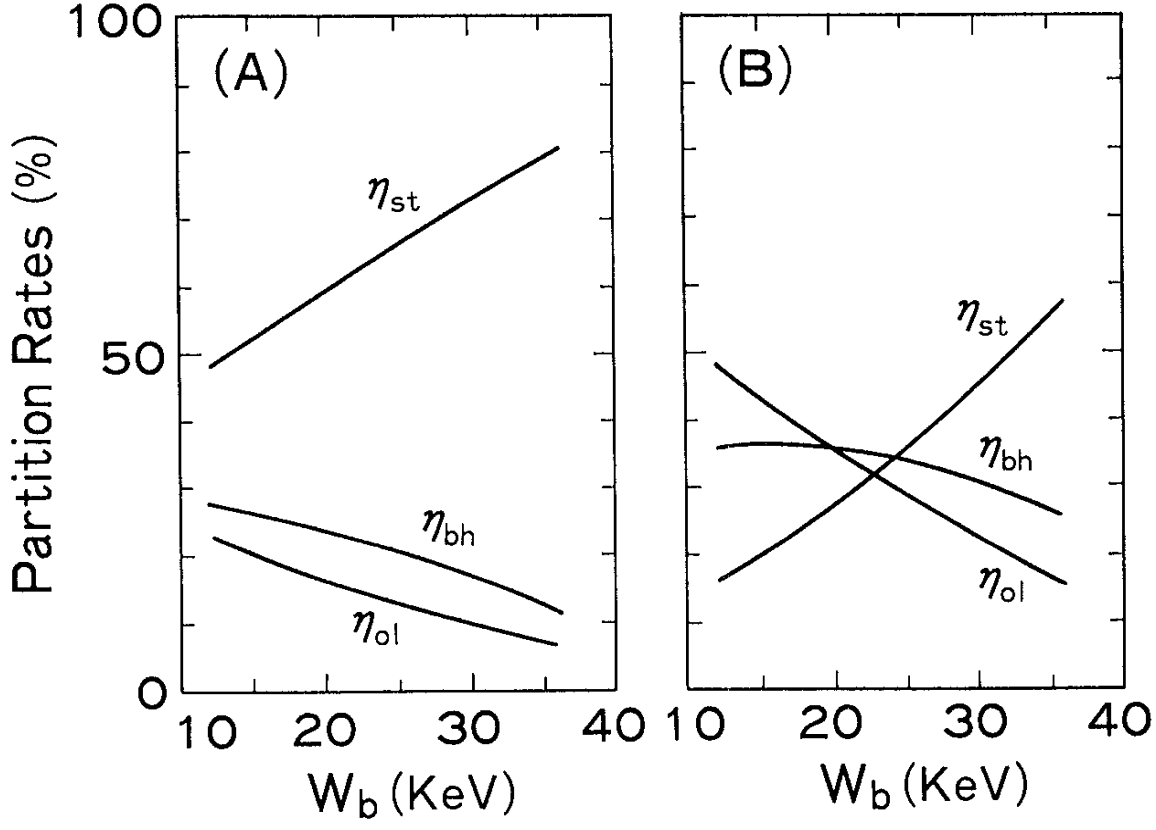
100
50
0
Partition Rates (%)
(A)
(B)
η_{st}
η_{bh}
η_{ol}
10
20
30
40
W_b (KeV)

Fig. 7

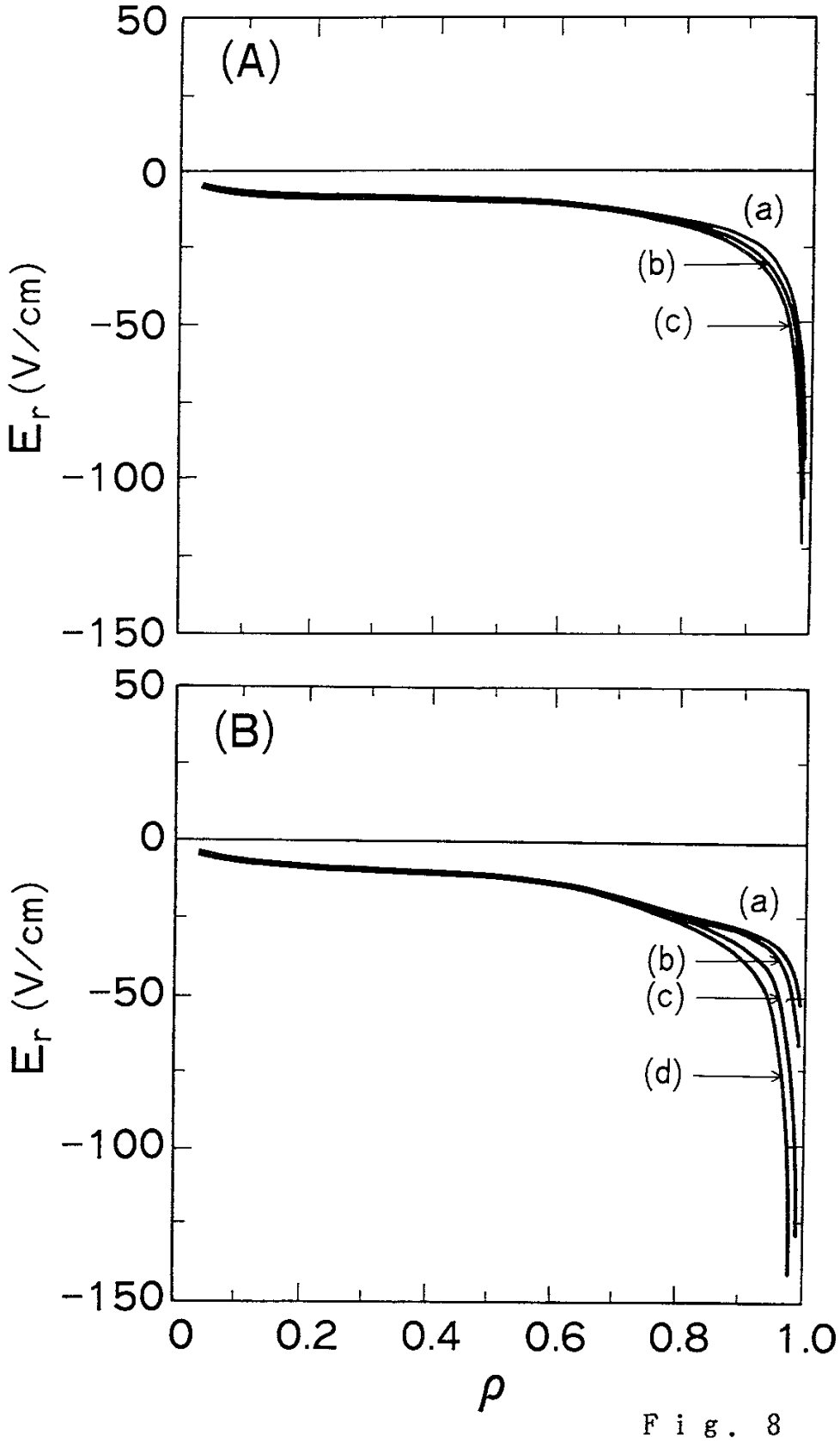

Fig. 8

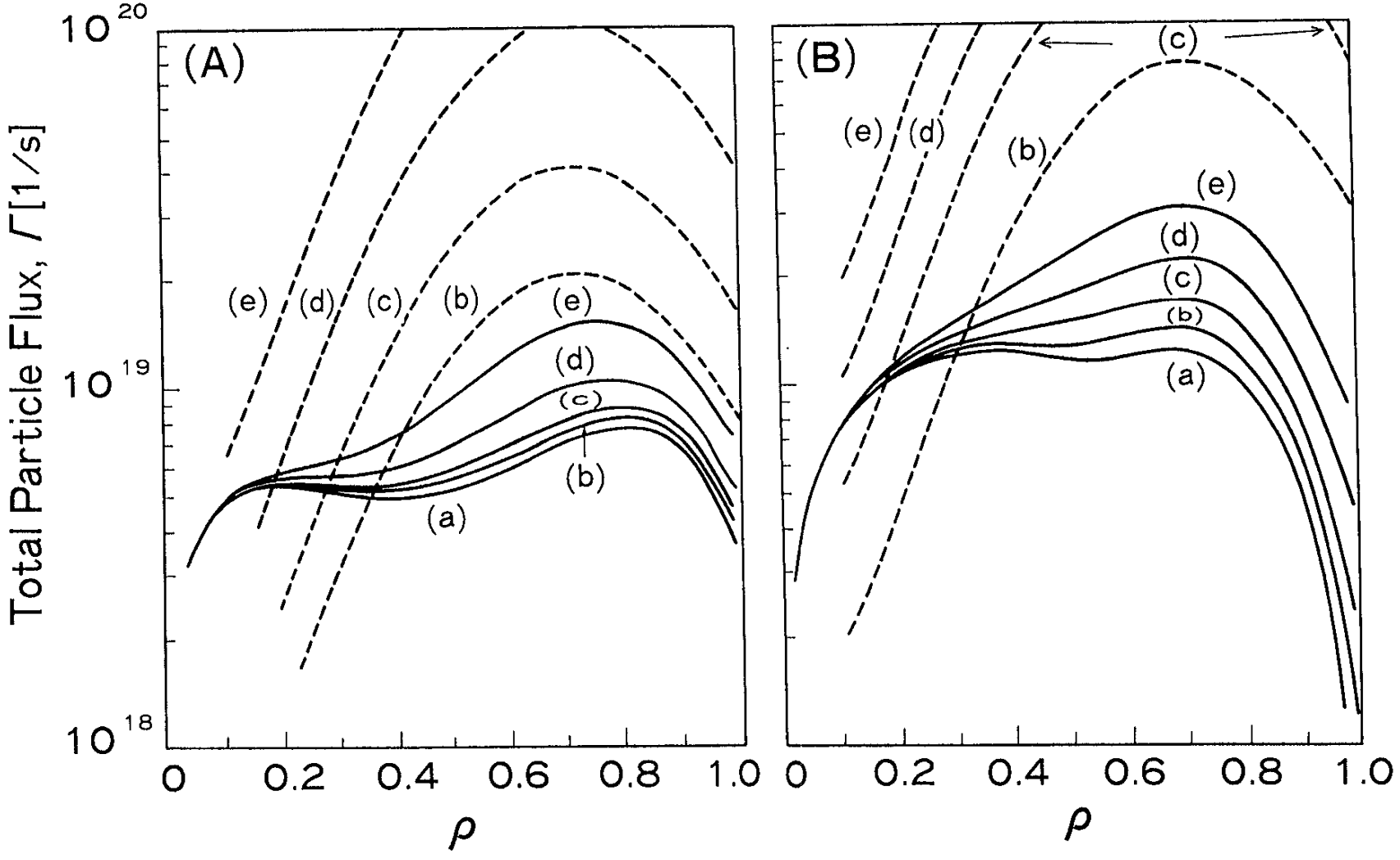
(A)
(B)
Total Particle Flux, Γ[1/s]
10^20
10^19
10^18
0
0.2
0.4
0.6
0.8
1.0
ρ
(a)
(b)
(c)
(d)
(e)

Fig. 9

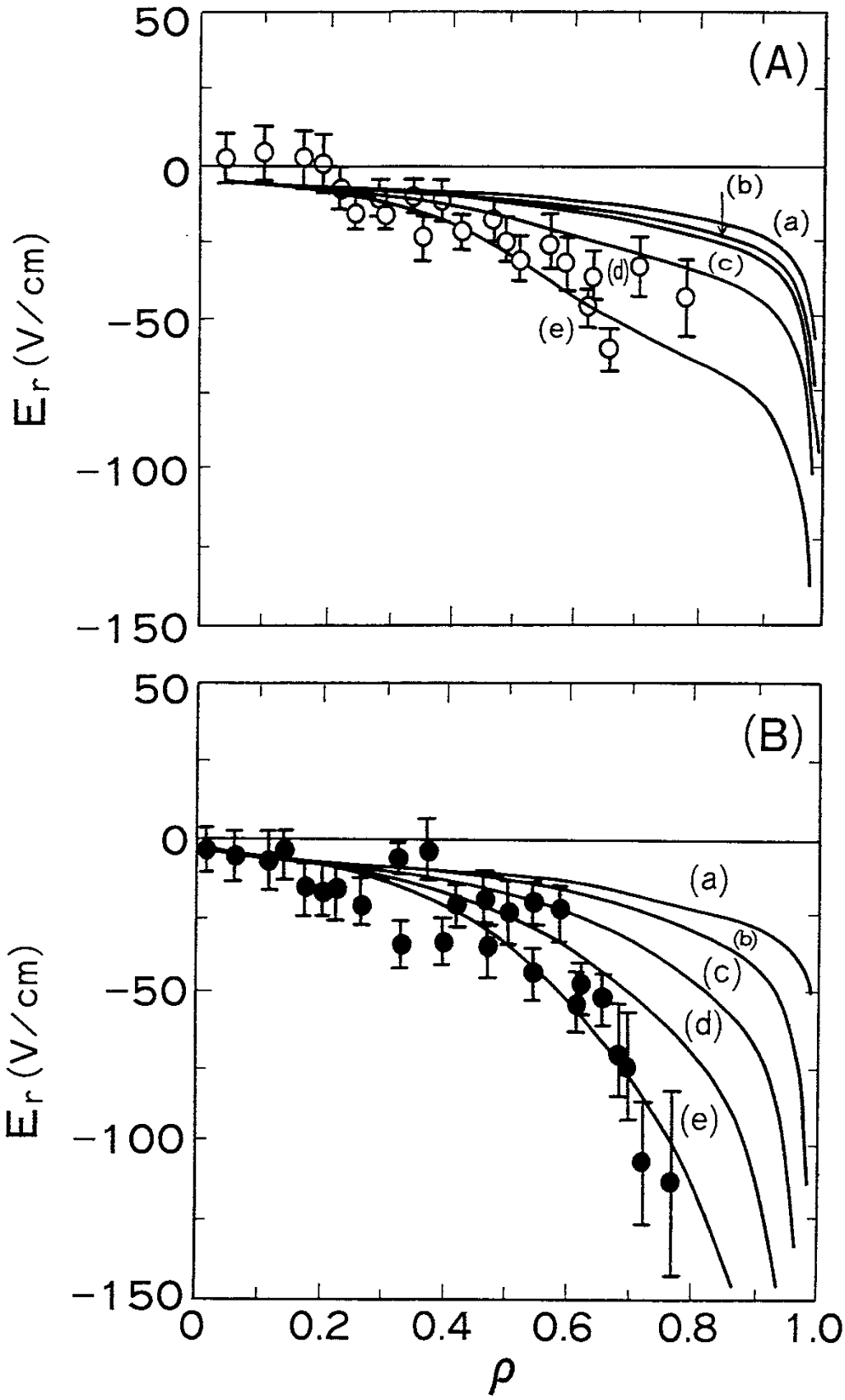

Fig. 10

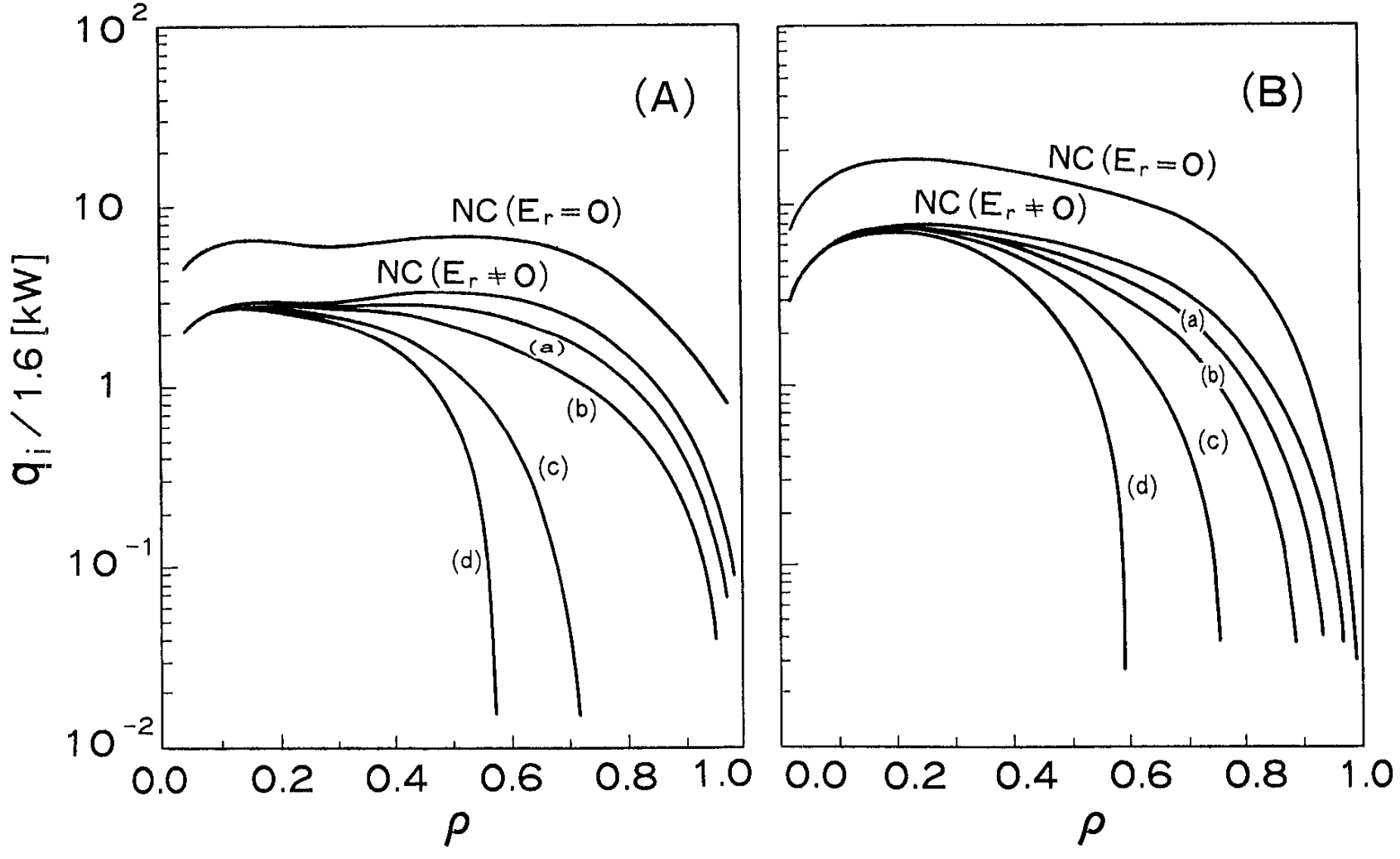

Fig. 11

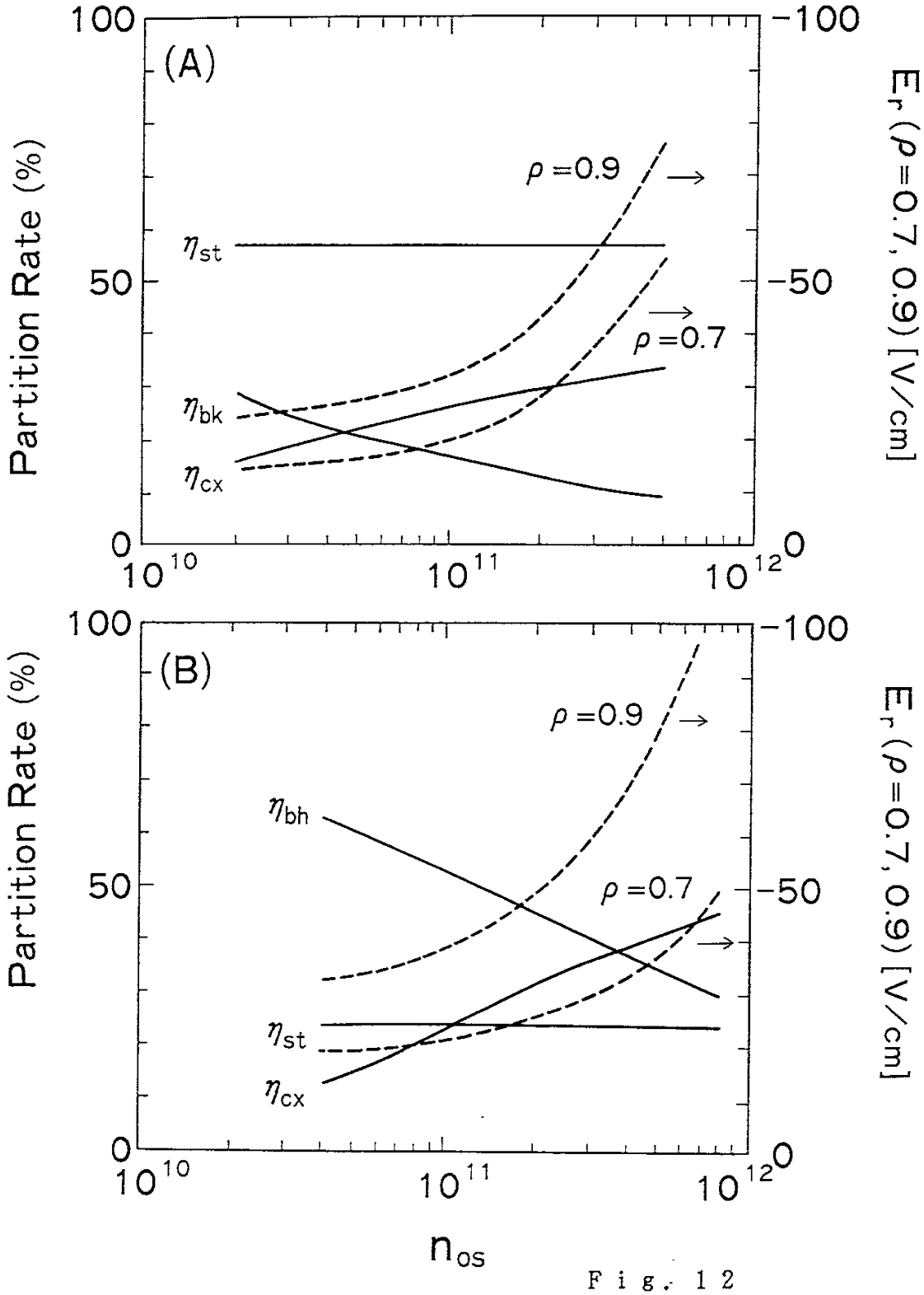
(A)
100
50
0
-100
-50
0
Partition Rate (%)
E_r (ρ=0.7, 0.9) [V/cm]
ρ =0.9
ρ =0.7
η_{st}
η_{bk}
η_{cx}
10^{10}
10^{11}
10^{12}
(B)
η_{bh}
η_{st}
η_{cx}
n_{os}

Fig. 12

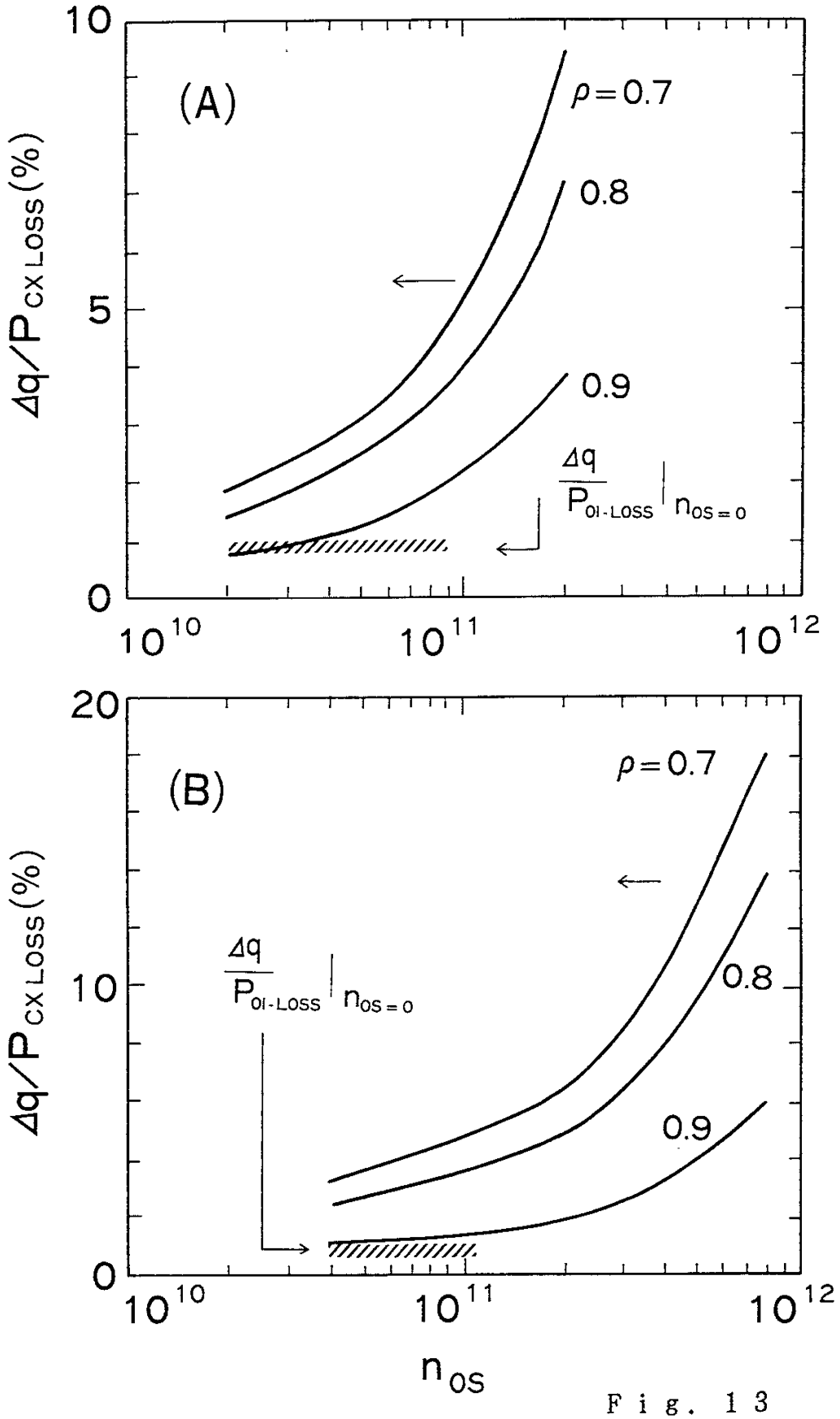
(A)
ρ=0.7
0.8
0.9
Δq/P_CX LOSS (%)
10
5
0
10^10
10^11
10^12
Δq / P_OI-LOSS | n_OS=0
(B)
ρ=0.7
0.8
0.9
20
10
0
n_OS

Fig. 13

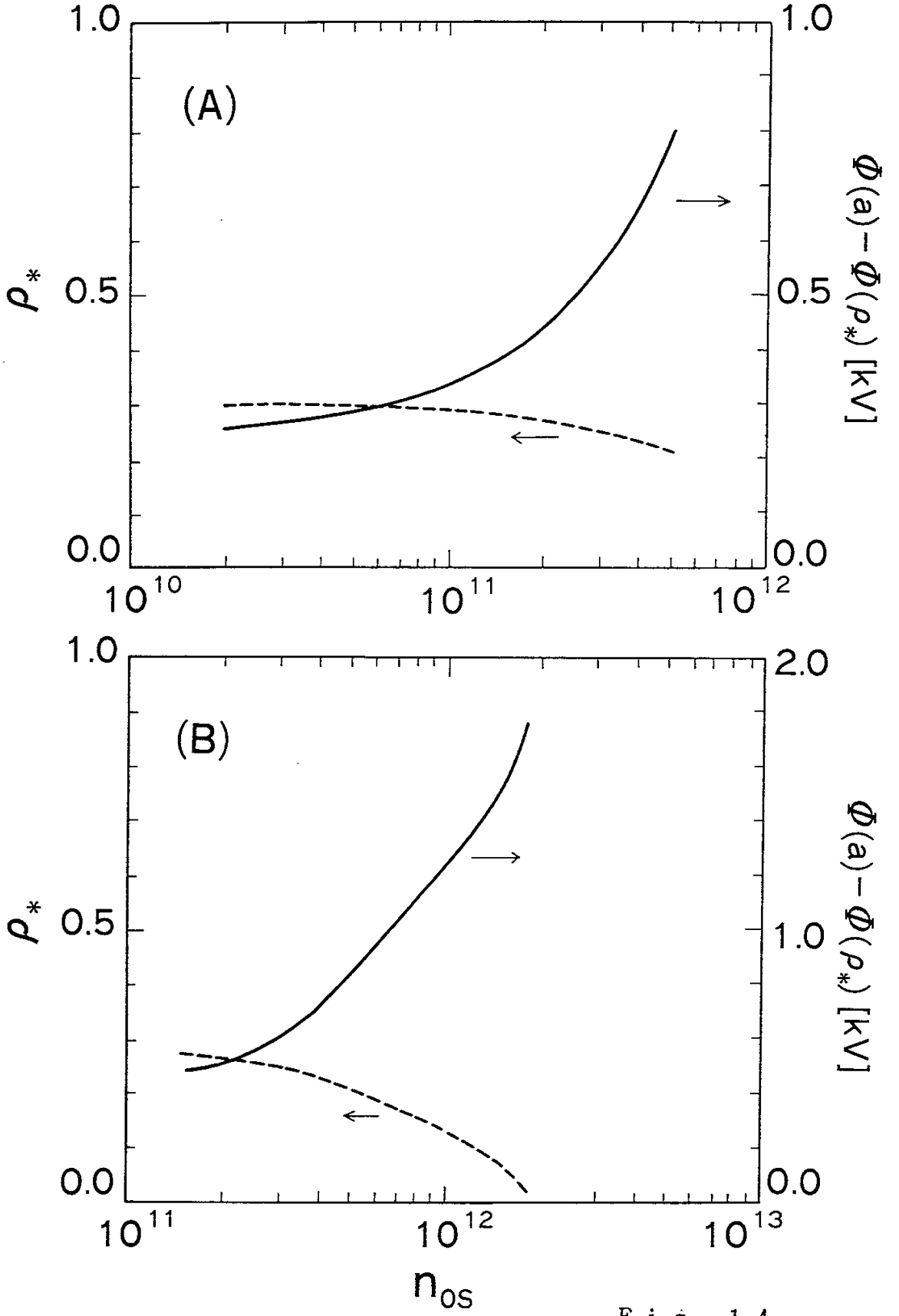

Fig. 14

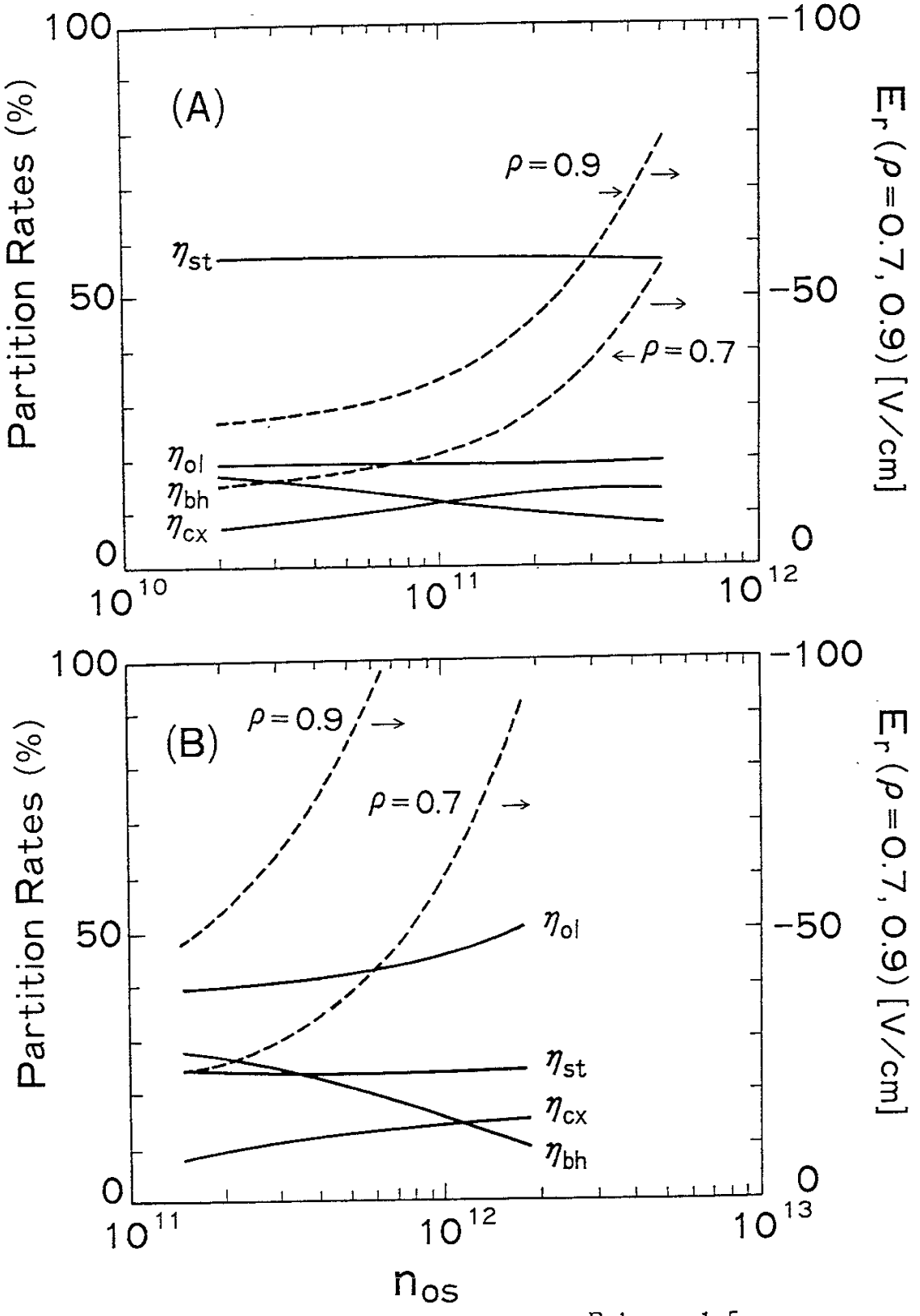
(A)
Partition Rates (%)
100
50
0
10^{10}
10^{11}
10^{12}
$\rho = 0.9$
$\rho = 0.7$
η_{st}
η_{ol}
η_{bh}
η_{cx}
$E_r(\rho = 0.7, 0.9)$ [V/cm]
-100
-50
0
(B)
Partition Rates (%)
100
50
0
10^{11}
10^{12}
10^{13}
n_{os}
$\rho = 0.9$
$\rho = 0.7$
η_{ol}
η_{st}
η_{cx}
η_{bh}
$E_r(\rho = 0.7, 0.9)$ [V/cm]
-100
-50
0

Fig. 15

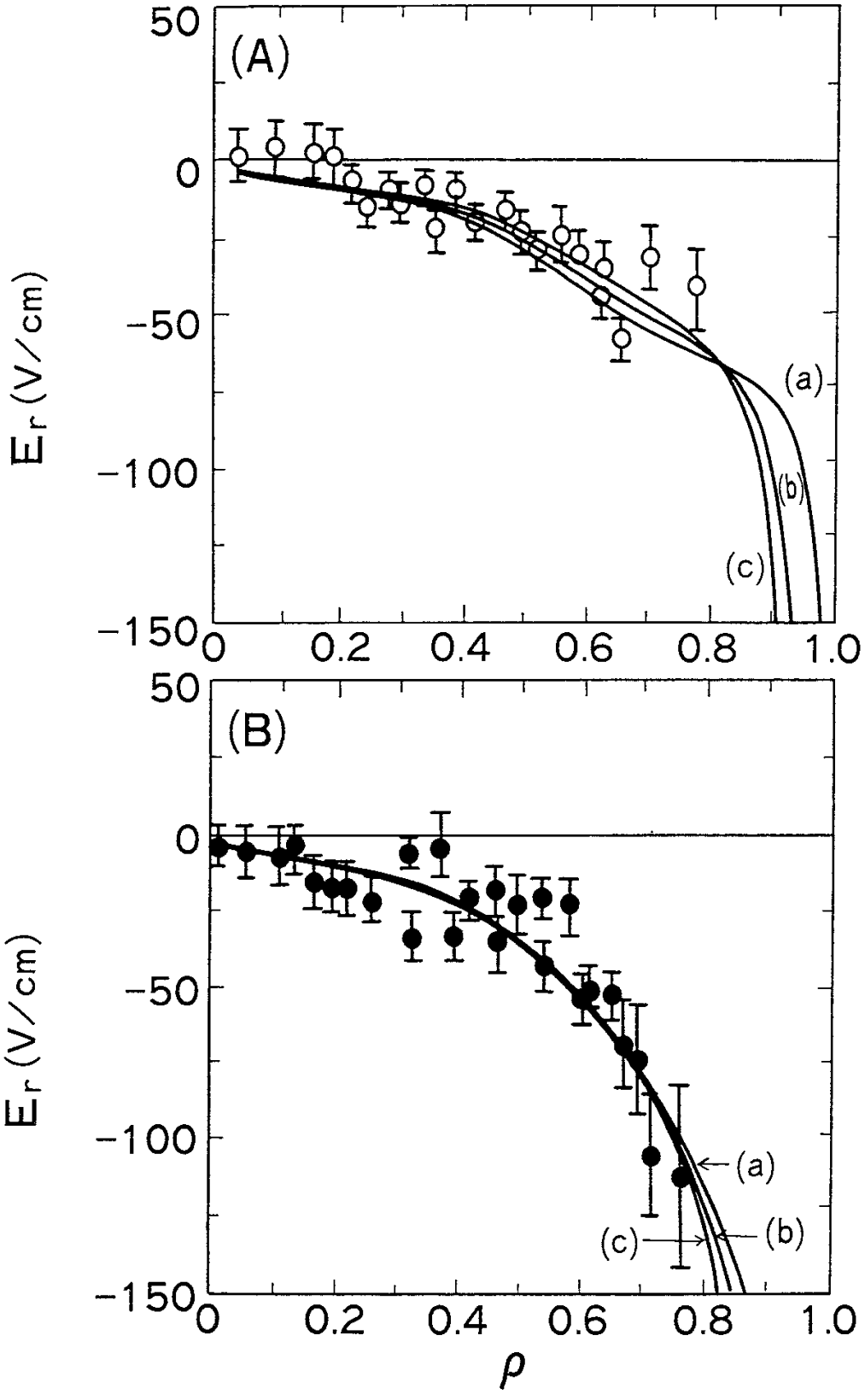

Fig. 16

Recent Issues of NIFS Series

NIFS-108 Y. Ogawa, T. Amano, N. Nakajima, Y. Ohyabu, K. Yamazaki, S. P. Hirshman, W. I. van Rij and K. C. Shaing, *Neoclassical Transport Analysis in the Banana Regime on Large Helical Device (LHD) with the DKES Code;* Sep. 1991

NIFS-109 Y. Kondoh, *Thought Analysis on Relaxation and General Principle to Find Relaxed State;* Sep. 1991

NIFS-110 H. Yamada, K. Ida, H. Iguchi, K. Hanatani, S. Morita, O. Kaneko, H. C. Howe, S. P. Hirshman, D. K. Lee, H. Arimoto, M. Hosokawa, H. Idei, S. Kubo, K. Matsuoka, K. Nishimura, S. Okamura, Y. Takeiri, Y. Takita and C. Takahashi, *Shafranov Shift in Low-Aspect-Ratio Heliotron / Torsatron CHS* ; Sep 1991

NIFS-111 R. Horiuchi, M. Uchida and T. Sato, *Simulation Study of Stepwise Relaxation in a Spheromak Plasma ;* Oct. 1991

NIFS-112 M. Sasao, Y. Okabe, A. Fujisawa, H. Iguchi, J. Fujita, H. Yamaoka and M. Wada, *Development of Negative Heavy Ion Sources for Plasma Potential Measurement* ; Oct. 1991

NIFS-113 S. Kawata and H. Nakashima, *Tritium Content of a DT Pellet in Inertial Confinement Fusion* ; Oct. 1991

NIFS-114 M. Okamoto, N. Nakajima and H. Sugama, *Plasma Parameter Estimations for the Large Helical Device Based on the Gyro-Reduced Bohm Scaling* ; Oct. 1991

NIFS-115 Y. Okabe, *Study of Au^- Production in a Plasma-Sputter Type Negative Ion Source* ; Oct. 1991

NIFS-116 M. Sakamoto, K. N. Sato, Y. Ogawa, K. Kawahata, S. Hirokura, S. Okajima, K. Adati, Y. Hamada, S. Hidekuma, K. Ida, Y. Kawasumi, M. Kojima, K. Masai, S. Morita, H. Takahashi, Y. Taniguchi, K. Toi and T. Tsuzuki, *Fast Cooling Phenomena with Ice Pellet Injection in the JIPP T-IIU Tokamak;* Oct. 1991

NIFS-117 K. Itoh, H. Sanuki and S. -I. Itoh, *Fast Ion Loss and Radial Electric Field in Wendelstein VII-Λ Stellarator*; Oct. 1991

NIFS-118 Y. Kondoh and Y. Hosaka, *Kernel Optimum Nearly-analytical Discretization (KOND) Method Applied to Parabolic Equations <<KOND-P Scheme>>;* Nov. 1991

NIFS-119 T. Yabe and T. Ishikawa, *Two- and Three-Dimensional Simulation*

Code for Radiation-Hydrodynamics in ICF; Nov. 1991

NIFS-120 S. Kawata, M. Shiromoto and T. Teramoto, *Density-Carrying Particle Method for Fluid* ; Nov. 1991

NIFS-121 T. Ishikawa, P. Y. Wang, K. Wakui and T. Yabe, *A Method for the High-speed Generation of Random Numbers with Arbitrary Distributions;* Nov. 1991

NIFS-122 K. Yamazaki, H. Kaneko, Y. Taniguchi, O. Motojima and LHD Design *Group, Status of LHD Control System Design ; Dec. 1991*

NIFS-123 Y. Kondoh, *Relaxed State of Energy in Incompressible Fluid and Incompressible MHD Fluid* ; Dec. 1991

NIFS-124 K. Ida, S. Hidekuma, M. Kojima, Y. Miura, S. Tsuji, K. Hoshino, M. Mori, N. Suzuki, T. Yamauchi and JFT-2M Group, *Edge Poloidal Rotation Profiles of H-Mode Plasmas in the JFT-2M Tokamak ;* Dec. 1991

NIFS-125 H. Sugama and M. Wakatani, *Statistical Analysis of Anomalous Transport in Resistive Interchange Turbulence* ;Dec. 1991

NIFS-126 K. Narihara, *A Steady State Tokamak Operation by Use of Magnetic Monopoles* ; Dec. 1991

NIFS-127 K. Itoh, S. -I. Itoh and A. Fukuyama, *Energy Transport in the Steady State Plasma Sustained by DC Helicity Current Drive* ;Jan. 1992

NIFS-128 Y. Hamada, Y. Kawasumi, K. Masai, H. Iguchi, A. Fujisawa, JIPP T-IIU Group and Y. Abe, *New Hight Voltage Parallel Plate Analyzer* ; Jan. 1992

NIFS-129 K. Ida and T. Kato, *Line-Emission Cross Sections for the Charge-exchange Reaction between Fully Stripped Carbon and Atomic Hydrogen in Tokamak Plasma*; Jan. 1992

NIFS-130 T. Hayashi, A. Takei and T. Sato, *Magnetic Surface Breaking in 3D MHD Equilibria of l=2 Heliotron* ; Jan. 1992

NIFS-131 K. Itoh, K. Ichiguchi and S. -I. Itoh, *Beta Limit of Resistive Plasma in Torsatron/Heliotron* ; Feb. 1992

NIFS-132 K. Sato and F. Miyawaki, *Formation of Presheath and Current-Free Double Layer in a Two-Electron-Temperature Plasma* ; Feb. 1992

NIFS-133 T. Maruyama and S. Kawata, *Superposed-Laser Electron Acceleration*

Feb. 1992

NIFS-134 Y. Miura, F. Okano, N. Suzuki, M. Mori, K. Hoshino, H. Maeda, T. Takizuka, JFT-2M Group, S.-I. Itoh and K. Itoh, *Rapid Change of Hydrogen Neutral Energy Distribution at L/H-Transition in JFT-2M H-mode ;* Feb. 1992

NIFS-135 H. Ji, H. Toyama, A. Fujisawa, S. Shinohara and K. Miyamoto *Fluctuation and Edge Current Sustainment in a Reversed-Field-Pinch;* Feb. 1992

NIFS-136 K. Sato and F. Miyawaki, *Heat Flow of a Two-Electron-Temperature Plasma through the Sheath in the Presence of Electron Emission;* Mar. 1992

NIFS-137 T. Hayashi, U. Schwenn and E. Strumberger, *Field Line Diversion Properties of Finite ß Helias Equilibria;* Mar. 1992

NIFS-138 T. Yamagishi, *Kinetic Approach to Long Wave Length Modes in Rotating Plasmas;* Mar. 1992

NIFS-139 K. Watanabe, N. Nakajima, M. Okamoto, Y. Nakamura and M. Wakatani, *Three-dimensional MHD Equilibrium in the Presence of Bootstrap Current for Large Helical Device (LHD);* Mar. 1992

NIFS-140 K. Itoh, S. -I. Itoh and A. Fukuyama, *Theory of Anomalous Transport in Toroidal Helical Plasmas;* Mar. 1992

NIFS-141 Y. Kondoh, *Internal Structures of Self-Organized Relaxed States and Self-Similar Decay Phase;* Mar. 1992

NIFS-142 U. Furukane, K. Sato, K. Takiyama and T. Oda, *Recombining Processes in a Cooling Plasma by Mixing of Initially Heated Gas;* Mar. 1992

NIFS-143 Y. Hamada, K. Masai, Y. Kawasumi, H. Iguchi, A. Fijisawa and JIPP T-IIU Group, *New Method of Error Elimination in Potential Profile Measurement of Tokamak Plasmas by High Voltage Heavy Ion Beam Probes;* Apr. 1992

NIFS-144 N. Ohyabu, N. Noda, Hantao Ji, H. Akao, K. Akaishi, T. Ono, H. Kaneko, T. Kawamura, Y. Kubota, S. Morimoto. A. Sagara, T. Watanabe, K. Yamazaki and O. Motojima, *Helical Divertor in the Large Helical Device;* May 1992

NIFS-145 K. Ohkubo and K. Matsumoto, *Coupling to the Lower Hybrid Waves with the Multijunction Grill;* May 1992

NIFS-146 K. Itoh, S. -I.Itoh, A. Fukuyama, S. Tsuji and Allan J. Lichtenberg, *A Model of Major Disruption in Tokamaks*; May 1992

NIFS-147 S. Sasaki, S. Takamura, M. Ueda, H. Iguchi, J. Fujita and K. Kadota, *Edge Plasma Density Reconstruction for Fast Monoenergetic Lithium Beam Probing*; May 1992

NIFS-148 N. Nakajima, C. Z. Cheng and M. Okamoto, *High-n Helicity-induced Shear Alfvén Eigenmodes*; May 1992

NIFS-149 A. Ando, Y. Takeiri, O. Kaneko, Y. Oka, M. Wada, and T. Kuroda, *Production of Negative Hydrogen Ions in a Large Multicusp Ion Source with Double-Magnetic Filter Configuration*; May 1992

NIFS-150 N. Nakajima and M. Okamoto, *Effects of Fast Ions and an External Inductive Electric Field on the Neoclassical Parallel Flow, Current, and Rotation in General Toroidal Systems*; May 1992

NIFS-151 Y. Takeiri, A. Ando, O. Kaneko, Y. Oka and T. Kuroda, *Negative Ion Extraction Characteristics of a Large Negative Ion Source with Double-Magnetic Filter Configuration*; May 1992

NIFS-152 T. Tanabe, N. Noda and H. Nakamura, *Review of High Z Materials for PSI Applications* ; Jun. 1992

NIFS-153 Sergey V. Bazdenkov and T. Sato, *On a Ballistic Method for Double Layer Regeneration in a Vlasov-Poisson Plasma*; Jun. 1992

NIFS-154 J. Todoroki, *On the Lagrangian of the Linearized MHD Equations*; Jun. 1992

NIFS-155 K. Sato, H. Katayama and F. Miyawaki, *Electrostatic Potential in a Collisionless Plasma flow Along Open Magnetic Field Lines;* Jun. 1992

NIFS-156 O.J.W.F.Kardaun, J.W.P.F.Kardaun, S.-I. Itoh and K. Itoh, *Discriminant Analysis of Plasma Fusion Data*; Jun. 1992

NIFS-157 K. Itoh, S.-I. Itoh, A. Fukuyama and S. Tsuji, *Critical Issues and Experimental Examination on Sawtooth and Disruption Physics*; Jun. 1992

NIFS-158 K. Itoh and S.-I. Itoh, *Transition to H-Mode by Energetic Electrons*; July 1992

NIFS-159 K. Itoh, S.-I. Itoh and A. Fukuyama, *Steady State Tokamak Sustained by Bootstrap Current Without Seed Current*; July 1992